Journal of Extracellular Vesicles

RESEARCH ARTICLE OPEN ACCESS

Endothelial Integrin-Linked Kinase (ILK) Deficiency Promotes Endothelial Activation and Cardiovascular Dysfunction via Receptor Interacting Protein Kinase-1 (RIPK1) Enriched-Extracellular Vesicle Signalling

Alberto Cook-Calvete[1,2] | María Delgado-Marín[1,2] | Sara Jorquera Ortega[1] | Silvia Moreta[1,2] | Mercedes Castro-Pinto[5,6] | José López-Menendez[5] | Blanca Fernandez-Rodriguez[1] | Julia García-García[1] | Carlos Zaragoza[2,3,4] | Marta Saura[1,2,3]

[1]Department of Systems Biology, Universidad de Alcalá, Alcalá de Henares, Madrid, Spain | [2]Ramón y Cajal Institute for Health Research (IRYCIS), Madrid, Madrid, Spain | [3]Cardiovascular Diseases Research Network Center (CIBERCV), Madrid, Madrid, Spain | [4]Francisco de Vitoria University, Pozuelo de Alarcón, Madrid, Spain | [5]Department of Cardiac Surgery, Ramón y Cajal Hospital, Madrid, Madrid, Spain | [6]Programa de Doctorado en Ciencias de la Salud, Universidad de Alcalá, Alcalá de Henares, Madrid, Spain

Correspondence: Marta Saura (marta.saura@uah.es)

Received: 18 July 2025 | **Revised:** 7 May 2026 | **Accepted:** 9 June 2026

Keywords: cardiac dysfunction | endothelial cell activation | extracellular vesicles | inflammation | integrin-linked kinase | microvascular remodelling | receptor interacting protein kinase 1

ABSTRACT

Integrin-linked kinase (ILK) maintains endothelial homeostasis by supporting endothelial nitric oxide synthase activity and restraining vascular inflammation. Although endothelial ILK loss is linked to vascular and cardiac disease, the mechanisms driving progression remain unclear. We hypothesized that extracellular vesicles (EVs) released by ILK-deficient endothelial cells propagate endothelial activation and cardiac dysfunction. In endothelial-specific ILK conditional knockout mice, ILK loss induced rapid endothelial activation, marked by increased iNOS, VCAM-1 and ICAM-1, followed by perivascular macrophage accumulation and chronic cardiac inflammation. In vitro, ILK-deficient endothelial cells exhibited barrier dysfunction, NF-κB activation and increased chemokine production. EVs derived from ILK deficient cells were enriched in pro-inflammatory cargo, including receptor-interacting protein kinase 1 (RIPK1), and transferred the activation phenotype to naïve endothelial cells. RIPK1 inhibition in recipient cells or RIPK1 silencing in donor cells abolished EV-induced activation, thereby confirming a necessary role for RIPK1. Endothelial ILK-deficient mice also exhibited increased circulating EVs enriched in endothelial activation markers and RIPK1. Transfer of these EVs to wild type mice induced coronary endothelial activation, macrophage recruitment, microvascular remodelling, cardiac fibrosis, and ventricular dysfunction mimicking the phenotype of the donor

Abbreviations: ApoE$^{-/-}$, apolipoprotein E knockout mice (atherosclerosis-prone model); CA, coronary atherosclerosis; CAEC, human coronary artery endothelial cells; Condition-EV, extracellular vesicles generated in vitro (condition = genotype and/or treatment); cEVs ^{condition}, circulating extracellular vesicles in vivo (condition = genotype, treatment or disease context); EC, endothelial cells; ecILK-cKO, endothelial cell-specific integrin-linked kinase conditional knockout; ecILK-cKO-EGFP, tamoxifen-inducible, endothelial-specific integrin-linked kinase conditional knockout mice carrying an EGFP (enhanced green fluorescent protein) reporter allele.; Endmt, endothelial-to-mesenchymal transition; ICAM-1, Intercellular Adhesion Molecule-1; IB4, isolectin B4; ILK, integrin-linked kinase; MAPK, Mitogen-Activated Protein Kinase; MCP-1, monocyte chemoattractant protein-1; nf-κb, nuclear factor kappa B; RIPK1, receptor-interacting protein kinase 1; VCAM-1, Vascular Cell Adhesion Molecule-1 .

Correction added on 21 July 2026, after first online publication: The author name was updated in the author list.

This is an open access article under the terms of the Creative Commons Attribution-NonCommercial-NoDerivs License, which permits use and distribution in any medium, provided the original work is properly cited, the use is non-commercial and no modifications or adaptations are made.

© 2026 The Author(s). *Journal of Extracellular Vesicles* published by Wiley Periodicals LLC on behalf of International Society for Extracellular Vesicles.

mice. RIPK1-dependent inflammatory effects were similarly observed with EVs from atherosclerotic ApoE^{-}/$^{-}$ mice and patients with coronary artery disease. These findings reveal an ILK–RIPK1 EV signalling axis that propagates vascular inflammation and promotes cardiac dysfunction, establishing a conserved pathogenic mechanism operative in experimental models and in human coronary artery atherosclerosis.

1 | Introduction

Endothelial dysfunction (ED) is a defining feature of many cardiovascular diseases (CVD), from atherosclerosis to hypertension (Xu et al. 2021, Zhang et al. 2023), and drives pathological processes such as vasoconstriction, intimal hyperplasia and inflammation (Xu et al. 2021). A central mechanism underlying ED is the loss of nitric oxide (NO) synthesis and bioavailability, a tightly regulated process that depends on cofactors such as tetrahydrobiopterin (BH4) and on protein partners, including the heat shock chaperone 90 (Hsp90) (Tuttolomondo et al. 2020). Among these regulatory proteins, integrin-linked kinase (ILK) has been identified as a key modulator of endothelial function and homeostasis (Herranz et al. 2012).

ILK, a serine/threonine kinase that binds the cytoplasmic domain of β-integrins, plays multifaceted roles in the heart, including its involvement in post-myocardial infarction (MI) remodelling (Lu et al. 2017, Zhang and Guo 2018). As a key regulator of multiple intracellular signalling pathways, ILK influences processes such as angiogenesis, mechanotransduction, extracellular matrix signalling and cellular responses, including survival, proliferation, differentiation and apoptosis (Górska and Mazur 2022).

Beyond its established impact on cardiomyocyte contractility, recent studies have highlighted the cardioprotective role of ILK in the endothelium (White et al. 2006, Knöll et al. 2007). Endothelial ILK is essential for maintaining vasomotor tone by preventing eNOS uncoupling (Herranz et al. 2012). Through this mechanism, ILK preserves endothelial integrity and blocks the cascade of oxidative stress, hypertension, acute inflammation and atherosclerosis (Herranz et al. 2012). We have shown that ILK degradation in aortic endothelium during inflammation accelerates atherosclerotic disease progression, directly linking ILK loss to ED and vascular inflammation (Reventun et al. 2017). Moreover, our group demonstrated that endothelial ILK prevents endothelial-to-mesenchymal transition (EndMT), and that endothelial-specific ILK deletion leads to spontaneous ischemic events, cardiac dysfunction, and adverse remodelling driven by microvascular damage (Reventun et al. 2023). Although microvascular injury and inflammation are fundamental contributors to heart failure, the earliest events that trigger this damage remain poorly understood.

Extracellular vesicles (EVs) have recently emerged as potent mediators of the myocardial response to ischemia, largely by shaping inflammatory signalling (Loyer et al. 2018). EVs regulate immune cell function and contribute to diverse inflammatory disorders, acting as stable messengers capable of long-distance communication (Grange and Bussolati 2022, Taqueti and Di Carli 2018). For example, EVs released by TNFα-stimulated endothelial cells can carry interleukins 6 and 8 (IL-6, IL-8), and Intercellular Adhesion Molecule-1 (ICAM-1), enhancing inflammatory activation in recipient endothelial cells and promoting monocyte adhesion and migration (Hosseinkhani et al. 2018). Increasing evidence also shows that necroptotic and inflammatory pathways drive the release of EVs enriched with necrosome-associated proteins, including Receptor-interacting protein kinase 3 (RIPK3) and Mixed Lineage Kinase Domain-Like protein (MLKL) (Gupta et al. 2022). The kinase receptor-interacting serine/threonine kinase 1 (RIPK1), a master regulator of cell survival, death and inflammation, plays a central role in these pathways (Ofengeim and Yuan 2013). While its scaffold function activates NF-κB and MAPK signalling, its kinase activity initiates RIPK3-dependent necroptosis, an immunogenic form of cell death (Pasparakis and Vandenabeele 2015). Thus, EVs released under inflammatory or death-inducing conditions may carry a mixture of cytokines, chemokines, adhesion molecules, and necroptosis-related proteins that can amplify immune activation and propagate inflammatory damage.

In this study, we hypothesized that the cardioprotective actions of endothelial ILK rely on its ability to prevent the release of inflammatory EVs, thereby limiting downstream cardiac injury. Using endothelial cells from an endothelial-specific ILK conditional knockout (ecILK-cKO) mouse, we examined how ILK loss shapes endothelial behaviour and alters EV secretion. We evaluated the in vitro and in vivo consequences of administering EVs derived from ILK-deficient endothelial cells to wild-type mice to determine whether these EVs can drive cardiac inflammation and dysfunction. Finally, to strengthen the clinical relevance of our findings, we extended our analysis to an atherosclerosis mouse model and to patients with coronary artery atherosclerosis, examining the release of EVs and their ability to induce inflammatory changes in healthy endothelial cells.

2 | Material and Methods

A detailed listing of the reagents and antibodies used throughout the study is provided in Table S1.

2.1 | Mice

To investigate the role of endothelial ILK in the heart, we used Cdh5(PAC)CreER^{T2}/ILK$^{lox/lox}$ mice (Reventun et al. 2023), derived from the cross of two parental mice: (a) Cre recombinase fused to a modified estrogen receptor under the control of an endothelial cell-specific VE-cadherin promoter (Cdh5(PAC)CreER^{T2}) (Kusumbe et al. 2014); and (b) the ILK gene, with exons 1 and 2 flanked by loxP sites (ILK$^{lox/lox}$) (Grashoff et al. 2003). To induce gene deletion, tamoxifen (for ecILK cKO mice) or corn oil (for control; CT mice) was administered

20013078, 2026, 6, Downloaded from https://isevjournals.onlinelibrary.wiley.com/doi/10.1002/jev2.70335 by Spanish Cochrane National Provision (Ministerio de Sanidad), Wiley Online Library on [31/07/2026]. See the Terms and Conditions (https://onlinelibrary.wiley.com/terms-and-conditions) on Wiley Online Library for rules of use; OA articles are governed by the applicable Creative Commons License

intraperitoneally at 1.5 mg/d for 5 consecutive days. Mice were then evaluated 1 and 3 weeks after induction.

Ai40 (B6.Cg-Gt(ROSA)26Sortm40.1(CAG-aop3/EGFP)Hze/J) mice were purchased from Jackson lab #021188 (The Jackson Laboratory, USA). Ai40 conditionally expresses an improved Archaerhodopsin-3/EGFP fusion protein (ArchT-EGFP) from the endogenous Gt(ROSA)26Sor locus. Following Cre-mediated removal of the floxed-STOP cassette, ArchT-EGFP expression is observed in the CRE-expressing cells. Ai40 mice were crossed with the Cdh5(PAC)CreER^{T2}/ILK$^{lox/lox}$ mice, generating the ecILK-cKO-EGFP mice. The parental Cdh5(PAC)CreER^{T2} mice crossed with Ai40 mice were employed as controls (further referred to as CT-EGFP mice). When tamoxifen is administered intraperitoneally for 5 days, CT-EGFP mice will express EGFP (enhanced green fluorescent protein) in endothelial cells with intact ILK expression. In contrast, ecILK cKO-EGFP mice will express EGFP and lack endothelial ILK.

Wild-type C57BL/6 mice and ApoE$^{-/-}$ mice were purchased from The Jackson Laboratory. Atherosclerosis was induced in apoE$^{-/-}$ mice by feeding them a Western diet (42% fat, Harlan Teklad, TD88137) for 16 weeks. ApoE$^{-/-}$ mice used as controls were fed a regular diet.

All animal procedures complied with EU Directive 2010/63/EU and Recommendation 2007/526/EC, which are implemented under Spanish law through Royal decree 53/2013. The animal protocols were approved by the local ethics committees and the Animal Protection Area of the Comunidad Autónoma de Madrid (131.5/24). Twelve-week-old male mice, weighing ≈25 g, were used in the study. Animals were randomly assigned to control and treatment groups using a computer-generated randomization schedule.

2.2 | Human Study

This study complies with the ethical principles outlined in the 1975 Declaration of Helsinki and its subsequent amendments. All human studies were conducted with the approval of the ethics committee of the Ramón y Cajal University Hospital, under the code CEIC: 031/24, and all participants provided written informed consent.

Blood samples were collected in a 5-mL Citrate tube before the start of surgery from 15 patients with coronary artery disease (9 men with a mean age of 74 ± 6.6 years; 6 women with a mean age of 74 ± 8 years), all with a confirmed diagnosis based on clinical symptoms and the presence of severe coronary lesions requiring surgical intervention, as determined by left heart catheterization. Only patients with coronary artery disease without associated valvular disease were included. Exclusion criteria were: age under 18 years, moderate or severe infection, anti-inflammatory or immunosuppressive treatment, chronic kidney disease stage G3b–G5 according to KDIGO or on dialysis, alcohol consumption >40 g/day, history of cardiac surgery, estimated life expectancy <1-year, congestive heart failure, acute myocardial infarction within the past 6 months, pacemaker carriers, and patients with type 1 diabetes mellitus. Blood samples were also obtained from healthy controls, comprising 13 participants (mean age 66.6 ± 11.3 years); 7 were men. Patient clinical characteristics are displayed in Table S2.

2.3 | Cells

Murine aortic endothelial cells were isolated from the aortas of Cdh5-PAC-Cre^{ERT2}/ILK$^{lox/lox}$ mice following previously described protocols (Herranz et al. 2012). The cells were selected based on their expression of vascular endothelial cadherin (CD144; BD 560411) and subsequently purified using a flow cytometry cell sorter (FACSAria Fusion, BD, NJ; USA). The purity of the cell cultures was confirmed by confocal microscopy with double staining using Platelet Endothelial Cell Adhesion Molecule-1 (CD31)and CD144 antibodies. Cells were grown in DMEM-F12 from Cytiva (Marlborough, MA, USA). To induce ILK deletion, mouse-derived EC were treated with TXF at a concentration of 10^{-6}M for 3 days (hereafter cKO EC) or vehicle (hereafter Ctr EC), as described previously (Reventun et al. 2023). RAW 264.7 cells were purchased from ATCC (Manassas, VA, USA) and maintained in RPMI-1640 (Sigma–Aldrich, St. Louis, MO, USA). For some experiments, primary endothelial cells isolated from non-genetically modified C57BL/6 mice were used and are referred to hereafter as wild-type (WT) EC. For endothelial cells and RAW 264.7 cells, the medium was supplemented with 10% FBS (Thermo Fisher Scientific, Waltham, MA, USA) and antibiotic-antimycotic solution (Merck, Darmstadt, Germany). Human coronary artery endothelial cells (CAEC) were obtained from ScienCell Research Laboratories (Carlsbad, CA, USA) and cultured in Endothelial Cell Medium from Cytiva (Marlborough, MA, USA), with 10% FBS and 1% Endothelial Cell Growth Supplement, and 1% mL penicillin/streptomycin (Lonza, Basel, Switzerland). Cells were cultured in a humidified incubator at 37°C with 5% CO_2.

2.4 | Immunoblot

Protein extracts were obtained as previously described (Reventun et al. 2017). In brief, tissue specimens were homogenized in a lysis buffer, and the resulting protein mixtures were resolved via 4%–12% SDS-PAGE and transferred onto PVDF membranes (Bio-Rad, Hercules, CA, USA). After blocking, membranes were incubated with specific primary antibodies at 4°C, followed by the appropriate secondary antibodies. Immunoreactive bands were visualized using the Pierce Western Blotting Substrate, following the manufacturer's guidelines (Pierce, Waltham, MA, USA). The antibodies used, along with their references, are listed in Table S3.

2.5 | RT-qPCR

RNA extraction from endothelial cells was performed using TRIzol reagent (Invitrogen Corporation, Carlsbad, CA, USA) following the manufacturer's instructions. To synthesize complementary DNA (cDNA), 2 μg of total RNA was used in a 20 μL reaction volume, utilizing the High-Capacity cDNA Reverse Transcription Kit (Life Technologies, Carlsbad, CA, USA). Quantitative PCR (qPCR) was conducted using the SYBR Select Master Mix (Life Technologies, Carlsbad, CA, USA). The qPCR protocol adhered to standard cycling conditions for primers with

20013078, 2026, 6, Downloaded from https://isevjournals.onlinelibrary.wiley.com/doi/10.1002/jev2.70335 by Spanish Cochrane National Provision (Ministerio de Sanidad), Wiley Online Library on [31/07/2026]. See the Terms and Conditions (https://onlinelibrary.wiley.com/terms-and-conditions) on Wiley Online Library for rules of use; OA articles are governed by the applicable Creative Commons License

melting temperatures of ≥60°C, starting with UDG activation at 50°C for 2 min, followed by AmpliTaq DNA Polymerase, UP activation at 95°C for 2 min, 15 s of denaturation at 95°C, and annealing/extension at 60°C for 1 min. The list of primers used in this study is provided in Table S2.

2.6 | Endothelial Cell Function Assessment

2.6.1 | Cell Nuclei Extraction

Endothelial cell monolayers were washed twice with PBS at 4°C, then centrifuged, and the supernatant was discarded. Nuclear extraction was performed using the Abcam kit (ab113474; Cambridge, UK) following the manufacturer's protocol. Briefly, the cell pellet was resuspended in 1x pre-extraction buffer, incubated on ice, and centrifuged to separate the cytoplasmic extract. An extraction buffer was added for nuclear extraction, followed by incubation, vortexing and sonication, before centrifugation to collect the nuclear extract (Jain et al. 2020). Protein concentration was measured using a BCA assay.

2.6.2 | Endothelial Monolayer Permeability Assay

Ctr and cKO endothelial cells (5×10^4 cells per insert) were seeded into the upper chambers of 24-well Transwell inserts with a 0.4 μm pore size (Corning, NY, USA). Cells were cultured in DMEM for 72 h to allow monolayer formation and confluence. After this period, the medium in the upper chambers was replaced with DMEM containing 2 mg/mL FITC-Dextran (150 kDa; Sigma, USA), while the lower chambers were filled with DMEM. At 5, 15, 30, 60, 120, 480 and 960 min post-exposure, 50 μL of medium was collected from the lower chambers for fluorescence measurement. FITC-Dextran fluorescence intensity was measured using a microplate reader (FLUOstar Omega) at 490/520 nm, enabling precise quantification of endothelial permeability changes (McMillin et al. 2015). Cell-free inserts (without cells) were included as a positive control to determine maximal tracer diffusion. Under these conditions, FITC-dextran freely crossed the membrane, and values were used to normalize permeability to 100%.

2.6.3 | Adhesion of Raw 264.7 Cells in Co-Cultures With Endothelial Cells

Migration experiments were conducted using *Transwell* chambers with 8 μm pore polycarbonate membranes (Corning, NY, USA) (Bijnsdorp et al. 2013). Adhesion of RAW 264.7 macrophages to endothelial cells was performed in co-culture conditions. Ctr- and cKO-ECs were seeded onto glass coverslips placed in 24-well plates and grown to confluence. Subsequently, 5×10^4 RAW 264.7 macrophages were added to each well and allowed to adhere for 1 h under standard culture conditions. Non-adherent macrophages were removed by washing twice with pre-warmed PBS. Cells were then maintained in culture for an additional 48 h before fixation with 4% paraformaldehyde in PBS for 20 min at 4°C, followed by PBS washes. Coverslips were carefully retrieved and processed for immunofluorescence staining using antibodies against CD68 (Abcam, Cambridge, UK), CD86 (BD Biosciences, San Jose, CA, USA) and CD206 (BioLegend, San Diego, CA, USA). Fluorescence microscopy was used to visualize and quantify macrophage adhesion.

2.7 | Isolation and Purification of Extracellular Vesicles (EV)

The processing required for EV isolation depends on the specific application. Studies indicate that ultracentrifugation (UC) can compromise EV integrity due to the mechanical stress it imposes, potentially reducing their functionality in downstream assays (De Sousa et al. 2023). Additionally, UC has been reported to promote particle aggregation and co-precipitate contaminants (Liangsupree et al. 2021), including lipoproteins, thereby compromising the purity and biological activity of EV samples (Tauro et al. 2013, Guo et al. 2021). For this reason, UC was reserved for molecular assays, whereas size-exclusion chromatography (SEC) was used for functional evaluations.

2.7.1 | EV Isolation From Endothelial Cell Culture Supernatant

Mouse aortic endothelial cells isolated from Cdh5-CreER^{T2}/ILK$^{lox/lox}$ mice were treated with TXF to generate EVs from ILK-deleted endothelial cells (cKO-EVs), while control cells were treated with vehicle (VH) to obtain control EVs (Ctr-EVs). After 72 h of treatment, the culture media were replaced with EV-depleted medium. Following an additional 48 h incubation period, conditioned media containing endothelial-derived EVs were collected. Cells were maintained at ~80% confluence in 100-mm culture dishes, and approximately 9 mL of conditioned media was collected per plate.

The media was centrifuged at 2500 × *g* for 15 min at 4°C twice, to eliminate apoptotic bodies and cellular debris. The supernatant was subjected to ultracentrifugation at 100,000 × *g* for 2 h at 4°C using a SW32 Ti rotor (Beckman Optima L-80XP) and used for molecular experiments. The resulting pellet was washed with 8 mL of sterile, 0.22 μM filtered PBS and centrifuged again at 100,000 × *g* for 2 h at 4°C. For functional assays, the media was ultrafiltrated and pre-concentrated by tangential flow filtration (TFF) using Amicon Ultra-100K MWCO filters (UFC9100; Millipore, Burlington, MA, USA) before separating EV and soluble factors using SEC columns (qEV35; IZON, Christchurch, New Zealand). Fractions were collected carefully to achieve optimal separation, ensuring no co-elution of contaminants (Figure S1A). In general, EVs derived from cultured cells are denoted as condition-EV, where *condition* indicates the cellular context, including genotype (e.g. Ctr or cKO) and/or experimental treatment (e.g. siRNA-mediated silencing, cytokine treatment).

EV isolation from Blood Samples (circulating EV;cEV): Blood samples were collected weekly from the following mice: CT, ecILK-cKO, CT-EGFP, ecILK-cKO-EGFP, ApoE$^{-/-}$ and ApoE$^{-/-}$ mice fed a high-fat diet. In addition, in the human study, 10 mL of peripheral blood was obtained from healthy control subjects and from patients with coronary artery atherosclerosis (CA).

20013078, 2026, 6, Downloaded from https://isevjournals.onlinelibrary.wiley.com/doi/10.1002/jev2.70335 by Spanish Cochrane National Provision (Ministerio de Sanidad), Wiley Online Library on [31/07/2026]. See the Terms and Conditions (https://onlinelibrary.wiley.com/terms-and-conditions) on Wiley Online Library for rules of use; OA articles are governed by the applicable Creative Commons License

Blood from at least four animals was pooled weekly within each group to increase cEV yield for subsequent assays. The pooled blood samples were processed by two rounds of centrifugation at 2500 × *g* for 15 min to obtain platelet-poor plasma (PPP). The same procedure was followed when using human samples. cEV isolation was performed using SEC columns (qEV35; IZON, Christchurch, New Zealand) with 35 nm pore size, designed to separate particles ranging from 35 to 400 nm. This method is expected to effectively isolate EV while minimizing contamination by smaller particles, such as lipoproteins (e.g. LDL and HDL, <35 nm) (Guo et al. 2021). The EV fraction was divided for different purposes. A portion of the cEV was resuspended in filtered PBS to prepare cEV treatments for animal and in vitro experiments, ensuring sterile conditions. The remaining cEV, intended for molecular analyses, were washed with filtered PBS and ultracentrifuged twice at 100,000 × *g* for 2 h at 4°C (Figure S1B). Circulating EVs are denoted as $cEV^{condition}$, where *condition* indicates genotype or disease context.

2.8 | Characterization of EV

2.8.1 | Nanoparticle Tracking Analysis (NTA)

The size and concentration of EV were evaluated using nanoparticle tracking analysis (NTA) with the NanoSight NS300 system (Malvern Panalytical Ltd.). The instrument was equipped with a 532 nm laser and an automatic syringe pump, set to flow rates of 10–75 (Harvard Apparatus, Holliston, MA, USA). Measurements were conducted at 25°C using a CMOS camera with a shutter speed of 1259 and a gain of 366. Samples of EVs were diluted in 1 mL of 0.2-μm-filtered PBS and analysed using a 488 nm laser to track their Brownian motion for 11.54 s. This process was repeated at least five times, with three videos recorded per sample. Data on particle concentration and size distribution were processed using the NS XPLORER software (v1.0.8641.14).

2.8.2 | Transmission Electron Microscopy (TEM)

The isolated EV pools were resuspended in filtered PBS. For negative staining, carbon-coated collodion-nickel grids (400 mesh, Glider) were glow-discharged. A 15 μL aliquot of each sample was adsorbed onto the grids for 2 min. The grids were rinsed with Milli-Q water and stained with 2% aqueous uranyl acetate (Electron Microscopy Sciences) for 1 min, then air-dried at room temperature. The grids were examined using a JEOL JEM-1210 transmission electron microscope operated at 120 kV. Images were acquired using a Gatan OneView digital camera at various magnifications. The vesicle diameters (both outer and inner) of 20 vesicles per sample were measured using Digital Micrograph software (version 3.51.3720.0; Gatan Inc., Pleasanton, CA, USA). Measurements were taken exclusively on vesicles with clearly defined borders.

2.8.3 | Western Blotting for EV Markers

EV enrichment was performed as previously described. To standardize loading, equal protein volumes were used. The lysates were centrifuged at 10,000 × *g* for 10 min at 4°C, and the resulting supernatant was quantified using the BCA assay (Thermo Fisher, 23225). For electrophoresis, 20 μg of total protein per sample, diluted in sample buffer, was heated at 95°C for 5> min and loaded onto Novex WedgeWell 4%–20% Tris-Glycine gels (Thermo Fisher Scientific, Waltham, MA, USA). Proteins were transferred using the Trans-Blot Turbo Transfer System (Bio-Rad Laboratories, Hercules, CA, USA) and visualized with Ponceau Red staining. Membranes were blocked in TBS-Tween 0.1% containing 5% bovine serum albumin (BSA) for 1 h at room temperature, followed by overnight incubation at 4°C with primary antibodies (diluted 1:500 in TBS-T containing 1% BSA). The exosome antibody panel (ab275018; Abcam, Cambridge, UK) included markers such as TSG-101, HSP70, CD9 and ITGB1. Membranes were washed with TBS-T, incubated with secondary antibodies (1:5000) for 1 h at room temperature, and subsequently developed with SuperSignal (Thermo Fisher Scientific, MA, USA). Images were acquired using the Bio-Rad Chemi-Doc system, and densitometric analysis was conducted using Fiji.app software (National Institutes of Health, Bethesda, MD, USA).

2.8.4 | Zeta (ζ)-Potential Measurements

Measurements of ζ-potential were conducted using the ZetaView PMX 110 system (Particle Metrix, Mebane, NC) and its accompanying software (version 8.04.02). EV samples were diluted in filtered PBS at ratios of 1:20,000 to 1:300,000 to achieve a particle count of 50–300 per frame, optimized for Nano Tracking Analysis (NTA). The temperature was maintained at 25°C, and each measurement comprised five cycles with the high-sensitivity setting. Between three and ten measurements were performed per sample. An additional ten measurements were conducted on representative samples from each group as controls to ensure sample stability throughout the process. Camera settings remained consistent across all measurements, with sensitivity and shutter values set to 90 and 70, respectively. The manufacturer recommended using high sensitivity to enhance EV detection.

2.8.5 | Flow Cytometry

cEV were isolated from mouse and human plasma as previously described. For flow cytometry analysis, freshly isolated cEVs were incubated with anti–VE-Cadherin antibodies (BD Biosciences, USA) and an anti-RIPK1 primary antibody (R&D Systems, Minneapolis, MN, USA) for 1 h at room temperature with gentle rotation in permeabilization buffer. The samples were subsequently washed with filtered PBS, concentrated using Amicon Ultra 100K filters (Millipore, Burlington, MA, USA) to remove unbound antibodies by TFF, and incubated with an APC-conjugated anti-mouse secondary antibody (Thermo Fisher Scientific, Waltham, MA, USA) for 45 min in the dark. After a final washing step, cEV were resuspended in PBS and analysed using a MACSQuant Analyzer 10 Flow Cytometer (Miltenyi Biotec, Bergisch Gladbach, Germany). For cEV obtained from ec-EGFP reporter mice, endothelial-derived vesicles were identified directly by their intrinsic EGFP fluorescence. Flow cytometry acquisition parameters were in accordance with MIFlowCyt-

20013078, 2026, 6, Downloaded from https://isevjournals.onlinelibrary.wiley.com/doi/10.1002/jev2.70335 by Spanish Cochrane National Provision (Ministerio de Sanidad), Wiley Online Library on [31/07/2026]. See the Terms and Conditions (https://onlinelibrary.wiley.com/terms-and-conditions) on Wiley Online Library for rules of use; OA articles are governed by the applicable Creative Commons License

EV2020 recommendations, and data were processed using MACSQuantify and FlowJo (version 10.8.1).

2.8.6 | EV Proteomics Analysis

EVs were pooled and stored as dry pellets at −80°C and reconstituted in 100 mM TEAB. Protein concentrations were determined using a Qubit assay and adjusted to 1 µg/µL. Proteins were reduced and alkylated with Tris (2-carboxyethyl) phosphine and iodoacetamide, followed by acetone precipitation and centrifugation. Pellets were resuspended in 50 mM TEAB and digested overnight with trypsin. After drying, samples were reconstituted in 0.1% FA, sonicated, and centrifuged. Protein concentrations were re-measured using a NanoDrop spectrophotometer (Thermo Fisher Scientific, Waltham, MA, USA) and adjusted accordingly. Peptides were separated via UHPLC and analysed by LC-MS using a Q-Exactive HF-X mass spectrometer. Data analysis employed Proteome Discoverer (SEQUEST HT for protein identification; Percolator for validation) and label-free quantification using the Minora feature.

Database research was conducted using Mascot, MsAmanda, MsFragger and Sequest HT, with reference to the mus musculus UniProtKB database (Feb 2021, 20,378 sequences) and cRAP contaminants. The false discovery rate (FDR) was set at 1% for proteins and peptides. Quantification was based on unique + razor peptides and precursor abundance, normalized to the total peptide amount. Differentially enriched proteins were identified using fold change thresholds (≥25%), pairwise *t*-tests, and Benjamini–Hochberg-adjusted *p* values. Volcano plots were generated with Graph Prism 10.3.1. Gene Set Enrichment Analysis (GSEA) was performed using the GSEA v4.3.0 against the Hallmark gene set collection (MSigDB). Permutations were set to 1000. To account for multiple hypothesis testing, the FDR was calculated, and pathways with q-values <0.25 were identified as significantly enriched (Liberzon et al. 2015).

2.8.7 | EV-Cytokine Array

The Proteome Profiler Mouse Cytokine Array Kit (Catalog No. ARY006, Bio-Techne, USA) was used to assess cytokine profiles in endothelial cell-derived EV, evaluating cytokines carried or enriched within the vesicles themselves (Lee et al. 2021). Briefly, EVs were isolated from conditioned media as described previously. We measured the protein concentration of the isolated EVs using a BCA assay. For the cytokine arrays, we loaded 100 µg of EV protein. The assays were performed according to the manufacturer's instructions, quantified using Fiji.app, normalized to internal control spots, and finally analysed using GraphPad Prism (v8.0.1, GraphPad Software, USA).

2.8.8 | Multiplex Analysis of EV Epitopes by Flow Cytometry

Circulating EVs isolated from plasma, as described above, were analysed using the MACSPlex Exosome Kit (Miltenyi Biotec, Bergisch Gladbach, Germany). For each sample, 120 µL of the cEVs suspension were transferred into low-adhesion 0.5 mL microcentrifuge tubes, followed by the addition of 15 µL of MACSPlex Exosome Capture Beads. Samples were incubated overnight at 4°C under continuous agitation (450 rpm) to allow cEV binding to the bead panel.

Bead–EV complexes were washed with MACSPlex buffer by centrifugation at 3000 × *g* for 5 min, and the supernatant was removed. For surface marker detection, APC-conjugated antibodies specific for CD9, CD63 and CD81 (5 µL each, provided in the kit) were added to reach a final reaction volume of 135 µL and incubated for 1 h at 450 rpm at room temperature. Samples were then washed twice with MACSPlex buffer and resuspended for flow cytometric acquisition.

Data were acquired on a MACSQuant Analyzer 10 (Miltenyi Biotec, Bergisch Gladbach, Germany) and processed using FlowJo (version 10.5.3). Gates corresponding to the individual capture bead subsets were adjusted. Median fluorescence intensities (MFIs) for each of the 39 bead populations were corrected by subtracting the corresponding values obtained from matched non-EV control media and normalized as suggested by the kit using the mean fluorescence intensities of CD9, CD63 and CD81. Results were analysed in FlowJo (v. 10.10.0) to obtain median signal intensities for all EV surface markers (Welsh et al. 2024, Koliha et al. 2016).

2.9 | Study of EV Effects on Endothelial Cells

Recipient cells were treated for 48 h with (i) PBS, (ii) purified Ctr-EV (5 µg/mL) or (iii) purified cKO-EV (5 µg/mL). All treatments were prepared in a 1:1 mixture with medium containing 10% FBS.

2.9.1 | Cell Proliferation

Wild-type EC were seeded into 24-well plates and cultured to confluence. To synchronize the cell cycle, the cells were cultured in FBS-free DMEM/F12 medium 24 h (Zhang et al. 2024). Then, cells were treated with either PBS, Ctr-EV or cKO-EV for 24 h. Following treatment, cells were fixed with 4% paraformaldehyde in PBS for 20 min at 4°C, then washed twice with PBS. Fixed cells were stained with Ki67 to assess proliferation and counterstained with Hoechst (for nuclear visualization). Ki67-positive cells were quantified to calculate the cell proliferation ratio, expressed as the percentage of Ki67-positive cells relative to the total cell count for each condition. Data were analysed using fluorescence microscopy and the Fiji ImageJ software.

2.9.2 | Wound Healing

A wound-healing assay was conducted in 24-well plates, with 2×10^5 WT EC cells seeded per well. After 18 h of treatment with Ctr-EV or cKO-EV, a scratch wound was created in each well using a pipette tip held at 45°. Images were taken at baseline (t0) and subsequently at 2, 4, 8, 10, 12 and 24 h post-wounding. The scratch area at each time point was analysed using Fiji.app, and results

20013078, 2026, 6, Downloaded from https://isevjournals.onlinelibrary.wiley.com/doi/10.1002/jev2.70335 by Spanish Cochrane National Provision (Ministerio de Sanidad), Wiley Online Library on [31/07/2026]. See the Terms and Conditions (https://onlinelibrary.wiley.com/terms-and-conditions) on Wiley Online Library for rules of use; OA articles are governed by the applicable Creative Commons License

were expressed as the percentage of the open wound area relative to the initial wound size (Kadota et al. 2021).

2.9.3 | Angiogenesis

For the angiogenesis assay, mouse aortic WT EC cells were seeded onto Matrigel-coated p.96 plates. Cells were treated with PBS, Ctr-EV or cKO-EV. Images were captured at 0 h (baseline) and 8 h post-seeding to evaluate tube formation. Quantitative analysis of the total branching points was normalized to PBS treated cells by using Fiji.app. Results were used to assess the effects of EV treatment on endothelial cell angiogenic capacity (Wolf et al. 2022).

2.9.4 | Endothelial Permeability

WT EC (5×10^4 per insert) were seeded into the upper chambers of 24-well Transwell inserts with a 0.4 μm pore size (Corning Inc., Corning, NY, USA) and cultured in standard DMEM for at least 72 h to allow monolayer formation and confluence. Subsequently, Ctr-EV or cKO-EV were added to the upper chambers. After 24 h of EV exposure, endothelial permeability was assessed by measuring the fluorescence of FITC-Dextran (150 kDa; Sigma, USA), in the lower chamber as explained elsewhere (McMillin et al. 2015).

2.9.5 | Macrophage Migration

Migration experiments were conducted using transwell chambers with 8 μm pore polycarbonate membranes (Corning, NY, USA) (Bijnsdorp et al. 2013). Raw 264.7 macrophages were grown in the upper chamber and WT endothelial cells in the lower chamber. For the migration experiment, WT EC were pretreated with Ctr-EV or cKO-EV for 8 h. After 18 h of incubation, the transwell membranes were disassembled. Cells on the upper surface of the membranes were gently scraped off using a scalpel, and the lower surface was stained with Hoechst for 15 min. Migrated RAW 264.7 macrophages were quantified. Images of the membrane surface were captured using a fluorescence microscope at multiple randomly selected, non-overlapping fields per insert (a minimum of five fields).

Hoechst-positive nuclei were counted using Fiji.App software (NIH, USA) with a consistent threshold applied across all conditions. The average number of migrated cells per field was calculated for each insert. Data were expressed either as a fold change relative to the control condition.

2.9.6 | RIPK1 Inhibitor Treatment

Endothelial cells were pre-treated with 10 nM of the RIPK1 inhibitor RI-962 (Li et al. 2022), for 1 h before stimulation with EVs. Cells were subsequently incubated with EVs under standard culture conditions.

2.9.7 | RIPK1 Silencing and Cytokine Array

In a subset of experiments, CTr- and cKO-EC were transfected with 25 nM non-targeting siRNA (Si-Scramble; SiSc) or RIPK1-targeting siRNA (SiRIPK1) using Lipofectamine 2000 transfection reagent and Opti-MEM (Gibco, Waltham, MA, USA) for 6 h. Following transfection, cells were cultured in EBM-2 medium for 3 days under the experimental conditions. Supernatant was collected, and EVs were isolated. EVs were used to treat WT mouse aortic EC as described. A cytokine array was performed with the cell lysates as described above.

2.10 | In Vivo Study of the cEV Effect on Cardiovascular Function

Vesicles isolated from control and ILK-deficient donor mice at weeks 1, 2 and 3 were administered to healthy C57BL/6 recipient mice at a dose of 10^{11} circulating extracellular vesicles (cEVs) per injection. The doses were given every 48 days for 1 week. Intravenous injections were performed under anaesthesia. To mimic the temporal progression associated with ILK deficiency, cEVs collected at the end of week 1 were administered to wild-type mice during week 1; those collected at the end of week 2 were administered during week 2; and cEVs from week 3 were administered during week 3.

Cardiovascular function was assessed in recipient mice at baseline (pre-treatment) and at 1 week and 3 weeks after treatment with circulating EVs or PBS. Echocardiography and ECG evaluations were performed by a single experienced operator blinded to the treatment groups, and all data analyses were conducted blinded to minimize bias. Mice were euthanized at 1 week or 3 weeks after administration of tamoxifen, vehicle or cEV. Group sizes were determined based on prior experience (Reventun et al. 2023).

2.10.1 | ECG Recordings

Mice were anesthetized with isoflurane (1%–1.5%, 1 mL/min oxygen) to maintain a heart rate of approximately 400 bpm. Fine-needle electrodes (25G) were inserted subcutaneously at the armpits and groin and connected to an AC amplifier (Cyberamp, Axon Instruments). ECG leads were initially set to lead II. Signals were amplified 500 times, filtered between 1 and 100 Hz, digitized at 1000 Hz (Power 1401, CED, UK), and stored for offline analysis using Spike 2 software (CED, UK). In some cases, surface ECG recordings were performed using an EDAN SE 601 device (ASMEDIC, Spain).

2.10.2 | Echocardiography

Mouse hearts were imaged using a Vivid Q ultrasound system (12.5 MHz transducer) under 1.5% isoflurane anaesthesia, with heart rate maintained at approximately 400 bpm. Parasternal short-axis images were captured in B-mode for M-mode recordings, with the cursor placed perpendicular to the interventricular septum and left ventricle posterior wall. Key parameters, includ-

20013078, 2026, 6, Downloaded from https://isevjournals.onlinelibrary.wiley.com/doi/10.1002/jev2.70335 by Spanish Cochrane National Provision (Ministerio de Sanidad), Wiley Online Library on [31/07/2026]. See the Terms and Conditions (https://onlinelibrary.wiley.com/terms-and-conditions) on Wiley Online Library for rules of use; OA articles are governed by the applicable Creative Commons License

ing interventricular septum thickness (IVS), left ventricle internal diameter (LVID), posterior wall thickness (LVPW), ejection fraction (EF), fractional shortening (FS) and heart rate (HR), were calculated using the system's software (Wehrens 2000). Diastolic function was further evaluated using the Vevo3100 system (VisualSonics, Toronto, Canada) with the MX550 transducer, and data were analysed offline with VevoLab software (v5.7.1).

2.10.3 | Immunofluorescence

Tissue sections or cells were incubated with primary antibodies as previously described (Reventun et al. 2023). After thorough washing with PBS, samples were incubated with fluorescence-conjugated secondary antibodies for 1 h at room temperature. Sections and cells were then washed twice with PBS to remove unbound antibodies and mounted using Hoechst solution for nuclear staining. Fluorescent images were acquired using a Leica TCS SP8 confocal microscope (Leica Microsystems, Germany) equipped with a 60× oil-immersion objective (numerical aperture 1.4), providing high-resolution imaging for accurate analysis. Excitation was performed with 405-, 488- and 561-nm lasers, and emission was collected using standard filter settings. Acquisition parameters, including laser power, detector gain and exposure time, were kept constant across all samples to ensure reproducibility and allow assessment of data quality.

2.10.4 | En Face Staining

Aortas were extracted from C57BL/6 wild-type mice treated with EV. Aortic rings were cut into 30-μm-thick segments and incubated at 37° in a cell culture incubator in Endothelial Cell media with 20 μg/mL EVs for 24 h in the presence and absence of 0.17 μg/mL of RIPK1 inhibitor RI-962. Afterward, aortic segments were incubated with antibodies to RIPK1, VE-cadherin, CD-31 and ICAM-1-1. The rings were then washed three times, and the endothelial layer was visualized in *en face* preparations with a Leica TCS SP5 confocal microscope (Leica Microsystems, Wetzlar, Germany). Fluorescent images were captured at ×10 magnification. Hoechst 33258 was used to visualize nuclei. The intensity of endothelial RIPK1 and ICAM-1-1 staining was analysed using Fiji.app. Ten complete fields were analysed per vessel, with one image per field. The mean fluorescence intensity (MFI) of endothelial cells stained for ICAM-1-1 or RIPK1 was calculated for each ring and averaged across animals within each group. Untreated aortas were preincubated in PBS and used for background correction and as a negative control.

2.10.5 | Histology

Histological staining was performed according to previously established protocols (Reventun et al. 2023). Briefly, hearts were excised under 2% isoflurane anaesthesia, and 10% KCl was injected into the left ventricle to arrest them in diastole. After perfusing the heart with PBS and 4% paraformaldehyde, hearts were washed with ice-cold PBS and fixed in formalin for 24 h at 4°C, dehydrated, and paraffin-embedded. Tissue sections of 5 μm were deparaffinized, rehydrated, and stained with Masson´s trichrome (EMD Millipore Corporation, Billerica, Massachusetts) for vascular remodelling quantification and Sirius Red staining (Sigma–Adrich, St. Luis, Missouri) for total and perivascular fibrosis quantification.

2.10.6 | Morphometric Analysis

Quantification of myocardial fibrosis was carried out in sections stained with Sirius Red, where fibrotic tissue appeared red. Six non-overlapping fields were selected from the left ventricular myocardium, including the free wall and interventricular septum and the right ventricle. These areas were imaged at 10x magnification using a Leica microscope to ensure comprehensive coverage of the heart tissue. The extent of fibrosis was quantified using the Colour Threshold plugin in Fiji.app software, which calculates the proportion of red-stained area relative to the total myocardial area. Fibrosis results are presented as the mean percentage of the fibrotic area relative to the total heart area in each mouse.

To assess perivascular fibrosis, we examined myocardial regions stained with Masson's trichrome, focusing on transversely oriented myocytes and circularly sectioned arteries with lumen diameters ranging from 10 to 100 μm. At least ten cross-sections per mouse were analysed. Perivascular fibrosis was quantified by calculating the ratio of the fibrotic area surrounding the vessel to the total vessel area using NIS element D3.2 Nikon software (Nikon, Tokyo, Japan).

Vessel area, lumen area and diameters were manually measured as previously (Reventun et al. 2023). For this, Fiji.app software was used. Microvascular remodelling was assessed by averaging wall thickness (intima and media) from four measurements around each arteriole. Results are expressed as the ratio of wall thickness to lumen area for each size category. All morphometric measurements were performed in a blind manner.

2.11 | Statistical Analysis

Statistical analyses were conducted using R (version 4.3.2) and GraphPad Prism (version 10). Group comparisons were performed according to the study design. For comparisons between two groups, an unpaired two-tailed Student's *t*-test was used when assumptions of normality and equal variances were met; otherwise, the Mann–Whitney *U* test was applied. For comparisons among more than two groups, one-way analysis of variance (ANOVA) followed by Bonferroni's post hoc test was performed. When parametric assumptions were not satisfied, the Kruskal–Wallis test was used. The assumption of normality was assessed for each group using the Shapiro–Wilk test. All in vitro experiments were conducted at least three times independently. Data are presented as mean ± standard deviation (SD). Statistical significance was defined as $p < 0.05$ (*), $p < 0.01$ (**) and $p < 0.001$ (***).

20013078, 2026, 6, Downloaded from https://isevjournals.onlinelibrary.wiley.com/doi/10.1002/jev2.70335 by Spanish Cochrane National Provision (Ministerio de Sanidad), Wiley Online Library on [31/07/2026]. See the Terms and Conditions (https://onlinelibrary.wiley.com/terms-and-conditions) on Wiley Online Library for rules of use; OA articles are governed by the applicable Creative Commons License

3 | Results

3.1 | Endothelial-Specific ILK Deletion Induces Endothelial Activation and Myocardial Inflammation

To explore the pathological mechanisms underlying cardiac microvascular damage caused by ILK deletion, we used the endothelium-restricted ILK deletion mice (Cdh5(PAC)-CreER^{T2}/ILK $^{lox/lox}$) previously described (Reventun et al. 2023). We treated a group of 10–12-week-old mice with 1.5 mg/day/animal of tamoxifen to induce ILK deletion (ecILK cKO) or with vehicle as control (CT) for 5 days. We examined the cardiac endothelial inflammatory response in mice at 1 week and 3 weeks post-treatment, as indicated in Figure 1A. Immunofluorescence analysis demonstrated endothelial activation at 1-week post-deletion, with increased iNOS expression (a marker of acute inflammation) and VCAM-1 colocalizing with CD31+ endothelial cells (Figure 1B,C). By 3 weeks, the expression of inflammatory markers persisted, reflecting a progression toward chronic inflammation (Figure 1C). The co-localization of VCAM-1 with CD31, quantified using Mander's colocalization coefficient, was evident as early as 1 week and became more pronounced by 3 weeks. Progressive perivascular macrophage infiltration (CD68^{+} cells) was observed, with notable increases from 1 to 3 weeks post-ILK deletion (Figure 1D). At 1 week, macrophages were detected in perivascular regions, indicating an early immune response to endothelial activation. By 3 weeks, macrophage accumulation was substantially higher. Together, these results show that endothelial ILK deficiency triggers an early phase of endothelial activation and inflammation, leading to a chronic inflammatory state characterized by ongoing immune cell recruitment. Representative images are shown in Figure 1C,D, with full confocal datasets in Figure S2A,B, respectively.

To directly assess whether ILK deletion induces endothelial activation, we evaluated endothelial cell adhesion and permeability in primary aortic endothelial cells isolated from Cdh5-PAC-CreER^{T2}/ILK$^{lox/lox}$ mice. To induce ILK deletion, cells were treated with 4-hydroxytamoxifen (TXF), while vehicle-treated cells served as controls. Hereafter, these are referred to as cKO-ECs and Ctr-ECs, respectively (Figure 1E). Tamoxifen-induced loss of ILK decreased endothelial cell adhesion, indicating endothelial barrier dysfunction that could weaken vascular integrity (Figure S3A). Additionally, ILK deletion led to increased endothelial permeability at 1 h, strongly suggesting that early endothelial cell activation occurs following ILK deletion (Figure S3B).

To explore the proinflammatory signalling in ILK-deficient EC, we quantified chemokine expression via qPCR at day 3 post-deletion (Figure 1F). The analysis revealed significant upregulation of MCP-1, IL-6, and monocyte chemotactic protein 3 (CCL-7) transcripts, which are key drivers of monocyte/macrophage recruitment and endothelial activation. This effect was specific to ILK deletion, as TXF treatment of aortic endothelial cells isolated from non-genetically modified wild-type C57BL/6J mice (WT ECs) did not alter ICAM-1 nor ILK mRNA expression. In contrast, cKO-EC, which showed a substantial reduction in ILK protein expression 72 h after TXF treatment, had higher ICAM-1-1 levels than vehicle-treated control cells (Figure S3C).

Next, we performed a macrophage-to-endothelial cell adhesion assay using control or ILK-deficient EC and RAW 264.7 macrophages to evaluate the functional effects of endothelial cell activation. Figure 1G shows that RAW 264.7 cells exhibit increased adhesion to ILK-deficient endothelial cells compared to control EC. Additionally, these macrophages display a proinflammatory phenotype, as indicated by a higher proportion of RAW cells expressing the M1 marker cluster of differentiation 86 (CD86) than the M2 marker macrophage mannose receptor (CD206). This suggests that ILK deletion not only enhances macrophage adhesion but also promotes their activation into a proinflammatory state.

Western blot analysis of cytosolic and nuclear fractions of cKO-EC revealed a clear activation of the NF-κB signalling pathway. There was a significant nuclear translocation of p65, a hallmark of NF-κB activation in ILK-deleted EC (Figure S3D). Ctr-EC treated with TNF-α and LPS to promote inflammatory signalling served as positive controls. P65 activation and nuclear translocation in ILK-deficient cells were also evidenced by immunofluorescence staining for phosphorylated P65 (p-P65) (Figure S3E). In addition, inhibition of NF-κB signalling with the specific inhibitor BAY-117082 inhibited MCP-1 and ICAM-1 induction observed after ILK deletion (Figure 1H). Consistent with these findings, IκB levels were also reduced in ILK-deficient cells, further supporting activation of inflammatory signalling pathways (Figure S3C). Together, these results indicate that ILK-deficient endothelial cells acquire a proinflammatory phenotype, altering their function and creating a chemotactic environment that enhances immune cell recruitment and activation.

3.2 | ILK-Deficient Endothelial Cells Release EV With Proinflammatory Potential

Next, we investigated the role of the EVs released by Ctr-ECs (Ctr-EV) and cKO-ECs (cKO-EV). To ensure accurate isolation and purification, we characterized the vesicle populations using established large-EV and small-EV markers by Western blot. Both large-EV markers (integrin β 1; ITGB1 and heat shock protein 70; HSP70) and small-EV markers (Tetraspanin-29; CD9 and Tumor Susceptibility Gene 101; TSG101) were detected in Ctr-EV and cKO-EV, confirming the successful isolation of a heterogeneous EV population (Figure 2A). Nanoparticle tracking analysis (NTA) further revealed a significant increase in cKO-EV concentration compared with Ctr-EV (Figure 2B,C). EV released by Ctr-EC treated with the proinflammatory stimuli TNF-α/LPS (Ctr+TNF/LPS-EV) were also studied. Morphologically, endothelial cell-derived EV exhibited the expected characteristics of small EVs, including a double-membrane structure and diameters <200 nm. Although mean particle size did not differ between groups (Figure S4A), the modal particle size was modestly increased in cKO-EV and Ctr+ TNF/LPS-EV, suggesting subtle structural alterations under pro-inflammatory conditions (Figure 2B). ζ-potential measurements showed that cKO-EV possessed a significantly more electronegative surface charge than Ctr-EV, similar to Ctr+TNF/LPS-EV (Figure S4B), a feature that

20013078, 2026, 6, Downloaded from https://isevjournals.onlinelibrary.wiley.com/doi/10.1002/jev2.70335 by Spanish Cochrane National Provision (Ministerio de Sanidad), Wiley Online Library on [31/07/2026]. See the Terms and Conditions (https://onlinelibrary.wiley.com/terms-and-conditions) on Wiley Online Library for rules of use; OA articles are governed by the applicable Creative Commons License

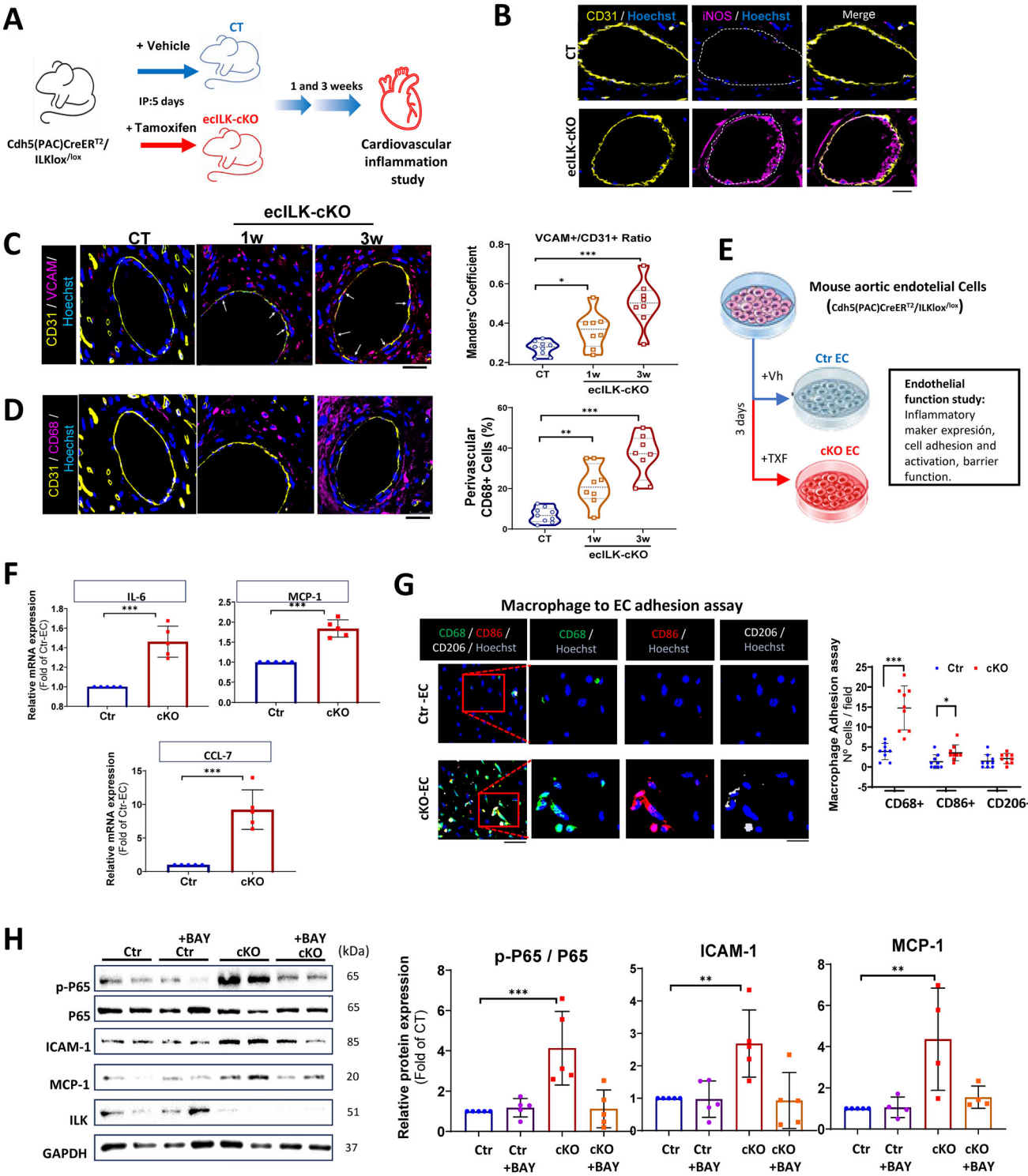

FIGURE 1 | Legend on next page.

may enhance vesicle–cell interactions and bioactivity. Moreover, normalization to cell number revealed that ILK-deficient cells released more EV than Ctr- or TNF-LPS-stimulated Ctr-ECs (Figure 2C).

Proteomic profiling via GSEA was performed to elucidate the molecular changes in EV cargo following ILK deficiency. The analysis revealed a significant positive enrichment of pathways categorized into three primary stress responses: inflammatory, oxidative and metabolic (Figure 2D). Specifically, EVs from ILK-deficient cells exhibited robust upregulation of key inflammatory mediators, including TNFα–NF-κB and IL-2–STAT5 signalling, as well as broader inflammatory signatures. Furthermore, pathways associated with oxidative stress such as reactive oxygen species (ROS) production, apoptosis, and peroxisome signalling, were significantly overrepresented. Metabolic stress markers, includ-

20013078, 2026, 6, Downloaded from https://isevjournals.onlinelibrary.wiley.com/doi/10.1002/jev2.70335 by Spanish Cochrane National Provision (Ministerio de Sanidad), Wiley Online Library on [31/07/2026]. See the Terms and Conditions (https://onlinelibrary.wiley.com/terms-and-conditions) on Wiley Online Library for rules of use; OA articles are governed by the applicable Creative Commons License

ing glycolysis and the hypoxia response, also showed consistent upregulation.

Notably, the Enrichment Score (ES) plots in Figure S4C show that genes involved in endothelial activation and oxidative stress are predominantly ranked toward the cKO-EV direction. EVs derived from ILK-deficient endothelial cells were significantly enriched for Hallmark gene sets related to inflammatory (Inflammatory response, TNF-α signalling via NF-κB) and metabolic (Glycolysis), and stress-response pathways (Hypoxia, Reactive oxygen species and UV response). Across all gene sets, enrichment scores were consistently positive at the leading edge in the cKO-EV condition, while genes associated with Ctr-EV were distributed toward the negative ranking metric region, supporting that endothelial ILK deficiency markedly alters EV protein cargo, favouring inflammatory, metabolic, and stress-adaptive pathways consistent with an activated endothelial state.

A volcano plot analysis of differentially expressed proteins in EVs derived from ILK-deficient endothelial cells (cKO-EVs) compared to control EVs (Ctr-EVs) revealed distinct molecular alterations (Figure 2E). Notably, RIPK1 was significantly upregulated in cKO-EVs. Given its well-established role in inflammatory signalling and necroptosis (Humphries et al. 2015), the enrichment of RIPK1 in cKO-EVs suggests that ILK deficiency enhances the transfer of pro-inflammatory mediators via EVs. Conversely, several complement-related proteins were downregulated (blue dots), consistent with previous reports describing suppression of complement pathways under conditions of cellular stress and activation (Ansari et al. 2021, Welsh et al. 2020, Karunakaran et al. 2021).

These proteomic findings were further validated by western blot analysis, confirming increased RIPK1 levels in EVs derived from ILK-deficient endothelial cells. In parallel, these EV samples exhibited elevated ICAM-1-1 and reduced ILK expression (Figure 2F), supporting a shift toward a pro-inflammatory EV cargo profile associated with ILK deficiency.

To extend these findings, we performed cytokine profiling of Ctr- and cKO-EVs, which revealed a marked enrichment of pro-inflammatory molecules in cKO-EV, including MCP-1 and ICAM-1-1 (Figure 2G). MCP-1 is a potent monocyte/macrophage chemoattractant (Deshmane et al. 2009), while ICAM-1 supports monocyte adhesion and transmigration (Ansari et al. 2021), indicating that cKO-EVs may potentiate immune cell recruitment.

These results indicate that cKO-EVs enhance inflammatory signalling by transporting pro-inflammatory cargo. Such changes in the secretory profile highlight the role of EV from ILK-deficient cells in driving endothelial inflammation and dysfunction.

3.3 | Extracellular Vesicles From ILK-Deficient Cells Impair Endothelial Function In Vitro

Next, we investigated whether cKO-EV could induce ED in Wild-type endothelial cells by conducting several functional assays. WT ECs treated with cKO-EV displayed a significant reduction in proliferation compared with PBS-treated cells (Figure S5A). In contrast, Ctr-EV increased EC proliferation compared with PBS-treated controls, suggesting that EVs derived from control ILK expressing-endothelial cells may support regenerative functions. Consistently, wound-healing assays showed impaired wound closure in cKO-EV-treated EC, whereas Ctr-EV enhanced their migratory capacity (Figure 3A). These results reveal a clear functional divergence between cKO- and Ctr-EV, with cKO-EV compromising the repair mechanisms. Angiogenesis assays further demonstrated that Ctr-EV promoted robust, organized vascular network formation, whereas cKO-EV exposure resulted in fragmented, disorganized structures, indicating a loss of angiogenic competence (Figures 3B and S5B). Lastly, barrier integrity and the inflammatory phenotype were examined. Endothelial barrier function was assessed by FITC–dextran permeability. cKO-EV-treated EC monolayers exhibited significantly increased permeability compared with Crl-EV-treated EC monolayers or PBS (Figure 3C).

Moreover, in a chemotaxis chamber, WT endothelial cells exposed to cKO-EV enhanced macrophage migration compared to Ctr-EV-treated cells (Figure 3D). cKO-EV also induced pronounced endothelial activation in WT endothelial cells, as reflected by increased protein expression of VCAM-1 and ICAM-1 (Figure 3E). This response was similar to that induced by EV derived from TNF-α/LPS-stimulated Ctr-EC, underscoring the clear pro-inflammatory potential of cKO-EV.

FIGURE 1 | Endothelial ILK deletion induces chronic cardiovascular inflammation. (A) Tamoxifen (TXF) regimen to induce endothelial ILK deletion in Cadherin 5(PAC)-CreER^{T2}-ILK $^{lox/lox}$ mice. Hearts were harvested at 1 and 3 weeks post-treatment. (B) Representative confocal images of a coronary artery in CT and ecILK-cKO mice at 1 week with the endothelium marker CD31 (yellow) and iNOS (magenta); nuclei (Hoechst, blue). Scale bar = 25 μm. (C) Representative immunofluorescence of coronary arteries stained for CD31 (yellow) and the activation marker VCAM-1 (magenta); nuclei (Hoechst, blue). Scale bar = 25 μm. VCAM-1/CD31 colocalization was quantified by Manders' coefficient (right panel). (D) Representative immunofluorescence of coronary vessels stained for CD31 (yellow) and CD68 (macrophages, magenta); nuclei (Hoechst, blue). Scale bars = 25 μm (10 μm inset). Right panel: Perivascular macrophage infiltration (CD68$^+$ cells within 10–20 μm of vessel wall). (E) Mouse endothelial cells were isolated from Cdh5-CreER^{T2}/ILK$^{lox/lox}$ mice and treated with vehicle (Ctr EC; ILK expression preserved) or Tamoxifen for 3 days to induce ILK deletion (cKO EC). Endothelial cell function parameters were studied. (F) qPCR analysis of Ctr and cKO ECs, assessing relative mRNA expression of monocyte-attracting and pro-inflammatory ligands ($n = 5$). (G) Representative confocal images showing enhanced macrophage adhesion to endothelial cells after ILK deletion. CD68 (macrophage marker; green), CD86 (M1 marker; red) and CD206 (M2 marker; white). Nuclei were stained with Hoechst in blue. Adhesion of RAW 264.7 macrophages to Ctr or cKO EC monolayers was quantified as the number of adherent macrophages per field. Scale bar = 10 μm and 25 μm in the amplification. (H) Immunoblot analysis of the p-P65, P65, ICAM-1, MCP-1 and ILK in Ctr and ILK-deleted EC treated with and without BAY-117085 (NF-kB inhibitor). Quantification of P65 phosphorylation, and ICAM-1, MCP-1 and ILK levels are displayed on the right panel. All data are presented as mean ± SD ($n \geq 4$). Statistical significance was determined using one-way ANOVA (*$p < 0.05$, **$p < 0.01$, ***$p < 0.001$).

20013078, 2026, 6, Downloaded from https://isevjournals.onlinelibrary.wiley.com/doi/10.1002/jev2.70335 by Spanish Cochrane National Provision (Ministerio de Sanidad), Wiley Online Library on [31/07/2026]. See the Terms and Conditions (https://onlinelibrary.wiley.com/terms-and-conditions) on Wiley Online Library for rules of use; OA articles are governed by the applicable Creative Commons License

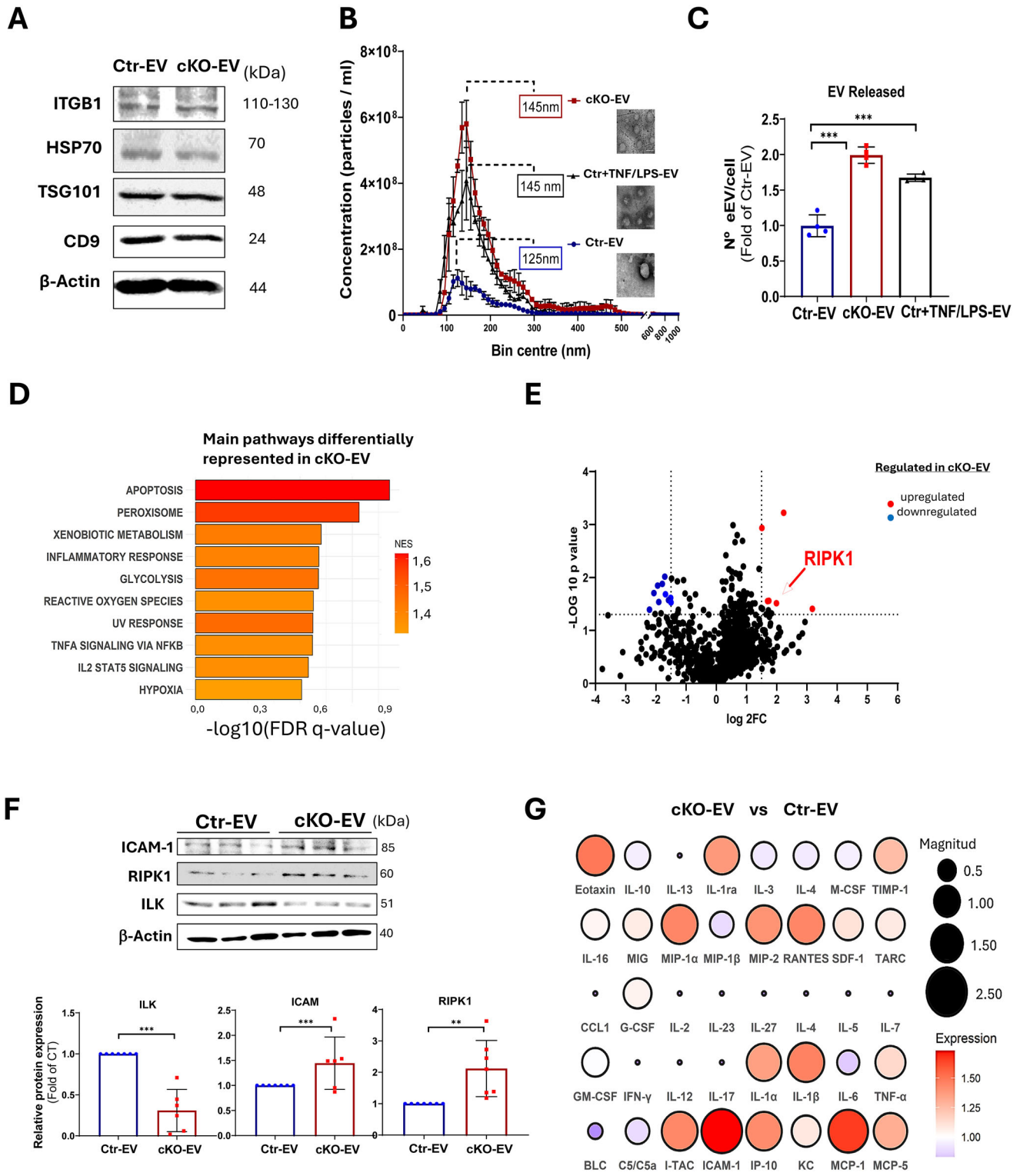

FIGURE 2 | Legend on next page.

Given the enrichment of RIPK1 in EVs from ILK-deficient endothelial cells, we next investigated whether RIPK1 is required for the biological activity of these EVs. WT EC were pretreated with the RIPK1 inhibitor RI-962 or left untreated, then exposed to PBS, Ctr-EV or cKO-EV. Pharmacological inhibition of RIPK1 signalling markedly reduced cKO-EV–induced NF-κB activation in WT EC, as evidenced by decreased p-P65 nuclear translocation (Figure 3F). To further confirm the role of RIPK1, we generated EVs from endothelial cells in which RIPK1 was either silenced (siRIPK1) or left unchanged using a scrambled control (SiScr), under both control (Ctr) and cKO conditions. These EVs were then applied to wild-type (WT) endothelial cells to evaluate their effects. RIPK1 silencing successfully reduced RIPK1 levels in both cKO endothelial cells (Figure S5C) and their derived EVs

20013078, 2026, 6, Downloaded from https://isevjournals.onlinelibrary.wiley.com/doi/10.1002/jev2.70335 by Spanish Cochrane National Provision (Ministerio de Sanidad), Wiley Online Library on [31/07/2026]. See the Terms and Conditions (https://onlinelibrary.wiley.com/terms-and-conditions) on Wiley Online Library for rules of use; OA articles are governed by the applicable Creative Commons License

(Figure S5D) compared with control cells treated with scrambled siRNA and their derived EV (Ctr-SiSc-EV). Importantly, EVs from RIPK1-silenced cKO cells no longer triggered the pro-inflammatory response normally induced by EVs from ILK-deficient cells, as shown by lower expression of inflammatory markers, particularly MCP-1 and ICAM-1 (Figure 3G).

Together, these findings demonstrate that loss of ILK drives the release of RIPK1-enriched EVs, and that RIPK1 is required for mediating the inflammatory signalling and ED induced by these vesicles, including inflammatory activation, impaired proliferation and migration and disrupted angiogenesis.

3.4 | Circulating EV Reflects Endothelial Activation

We next studied circulating EV (cEV) from endothelial ILK-deleted mice ($cEV^{ecILK\text{-}cKO}$) and control ILK-expressing mice (cEV^{CT}). cEVs were isolated weekly from the plasma of ecILK-cKO and CT mice for 3 weeks after TXF/Vehicle treatment and analysed as indicated (Figure 4A). Nanoparticle tracking analysis (NTA) of cEV revealed no significant differences in size distribution between cEV^{CT} and $cEV^{ecILK\text{-}cKO}$. In addition, transmission electron microscopy revealed comparable vesicle morphology across groups, consistent with preserved structural integrity (Figure S6A,B). In contrast, normalization to plasma volume showed a significant increase in total circulating EV abundance in ecILK-cKO mice compared with controls (Figure 4B), indicating enhanced EV release upon endothelial ILK deletion.

To determine whether this increase reflected changes in endothelial-derived vesicles, we quantified CD31-positive cEVs by flow cytometry. Surprisingly, despite the overall increase in total cEV abundance, the proportion of CD31+ cEVs was markedly lower in ecILK-cKO mice (31.4 ± 7.1%) than in control mice (85.8 ± 8.6%). To further analyse the cellular origin of the cEVs, we performed unbiased surface marker profiling. This analysis revealed that the cEV pool in both control and ecILK-cKO mice is composed primarily of vesicles derived from endothelial, platelet and immune cells. Importantly, a substantial fraction of cEVs in ecILK-cKO mice retained endothelial origin markers and displayed signatures consistent with endothelial activation (Figure 4C). Notably, the endothelial marker CD31 was significantly reduced within the endothelial EV signature in ecILK-cKO mice, consistent with the flow cytometry data. Endothelial ILK deficiency was also associated with the emergence of cEV populations enriched in immune cell–associated activation markers, whereas platelet-derived EV signatures remained unchanged compared with controls (Figure 4D). Together, these findings indicate that ILK loss does not reduce endothelial EV release but instead induces a profound remodelling of EV surface marker composition towards endothelial and immune activation profiles.

To further investigate the molecular cargo of circulating EVs, we performed a proteomic analysis and GSEA, which revealed significant enrichment for proteins associated with glycolysis, oxidative phosphorylation, and hypoxia in the $cEV^{ecILK\text{-}cKO}$ group compared to cEV^{CT} (Figure S6C,D). These pathways met the predefined exploratory significance threshold of FDR $q < 0.25$, with glycolysis and oxidative phosphorylation showing the strongest enrichment. In contrast, the complement pathway was negatively enriched in cKO-EVs, like the pattern observed in endothelial cell–derived EVs. Consistent with these findings, immunoblot analysis demonstrated that cEV from ecILK-cKO mice were enriched in endothelial activation markers, including VCAM-1, ICAM-1, and von Willebrand factor (vWF), as well as the inflammatory kinase RIPK1 (Figure 4E). Since these proteins are closely linked to vascular inflammation and ED (Ansari et al. 2021), their enrichment in cEV supports the idea that endothelial ILK loss promotes the release of EVs with a pro-inflammatory cargo profile.

To directly trace the endothelial contribution to the circulating EV pool, we generated an endothelial-specific ILK–EGFP reporter mouse (ecILK cKO-EGFP) by crossing Cdh5(PAC)-$CreER^{T2}$/$ILK^{lox/lox}$ mice with Ai40D reporter mice, in which Cre recombination induces endothelial EGFP expression. Control reporter mice (CT-EGFP) were generated by crossing Cdh5(PAC)-$CreER^{T2}$ with Ai40D mice (Figure 4F). Immunofluorescence confirmed robust, specific endothelial EGFP expression, validating this model for lineage tracing. In addition, endothelial ILK

FIGURE 2 | Characterization of EVs from ILK-deficient endothelial cells. (A) Representative Immunoblot of EV markers (ITGB1, HSP70, CD9 and TSG101) present in EV isolated form Ctr EC (Ctr-EV) and ILK deleted EC (cKO-EV) ($n = 3$). (B) Nanoparticle Tracking Analysis (NTA) of EV derived from Ctr and cKO EC and Ctr cells stimulated with TNFα+LPS as a positive control of inflammatory stimuli (Ctr+TNF/LPS). Representative Transmission Electron Microscopy (TEM) images of EVs illustrating their typical morphology and size are shown on the right. Scale bar = 100 nm. (C) Quantification of the number of EV released per condition, as determined by NTA analysis and normalized to Ctr-EV. (D) Gene Set Enrichment Analysis (GSEA) of inflammatory pathways enriched in cKO-EV compared to Ctr-EV. Each panel represents a predefined biological pathway (blue), and the analysis tests whether genes belonging to that pathway tend to occur disproportionately at the top or bottom of a ranked list of genes between the two conditions (cKO-EV vs. Ctr-EV). The green curve shows the running enrichment score, black vertical bars indicate the positions of pathway genes in the ranked list, and the red/blue colour scale reflects genes upregulated in cKO-EV (left/red) or Ctr-EV (right/blue). Positive enrichment scores, therefore, indicate that pathway-associated genes are predominantly upregulated in cKO-EV. Pathways shown met the threshold of FDR q-value < 0.25. (E) The volcano plot illustrates differentially expressed molecules in cKO-EV compared to Ctr-EV. The x-axis represents the $\log_2$ fold change ($\log_2$FC), indicating the relative abundance of molecules, while the y-axis represents the $-\log_{10}(p\text{ value})$, showing statistical significance (p value <0.05). Molecules with significant downregulation in cKO-EV are highlighted in blue, while significantly upregulated molecules are shown in red, such as RIPK1, a key regulator of necroptosis and inflammation. (F) Western blot analysis of the ICAM-1, RIPK-1, and ILK in Ctr- and cKO-EV to validate the results of the proteomic analysis ($n \geq 6$). (G) Heatmap representing the cytokine profile ratio in EVs (cKO-EV to CTr-EV). Cytokines are colour-coded by expressions: red indicates upregulation, blue indicates downregulation, and white indicates no significant change. All data are presented as mean ± SD from at least four independent experiments. Statistical significance was determined using one-way ANOVA and Student's t-test; $^{**}p < 0.01$, $^{*}p < 0.001$ versus control.

20013078, 2026, 6, Downloaded from https://isevjournals.onlinelibrary.wiley.com/doi/10.1002/jev2.70335 by Spanish Cochrane National Provision (Ministerio de Sanidad), Wiley Online Library on [31/07/2026]. See the Terms and Conditions (https://onlinelibrary.wiley.com/terms-and-conditions) on Wiley Online Library for rules of use; OA articles are governed by the applicable Creative Commons License

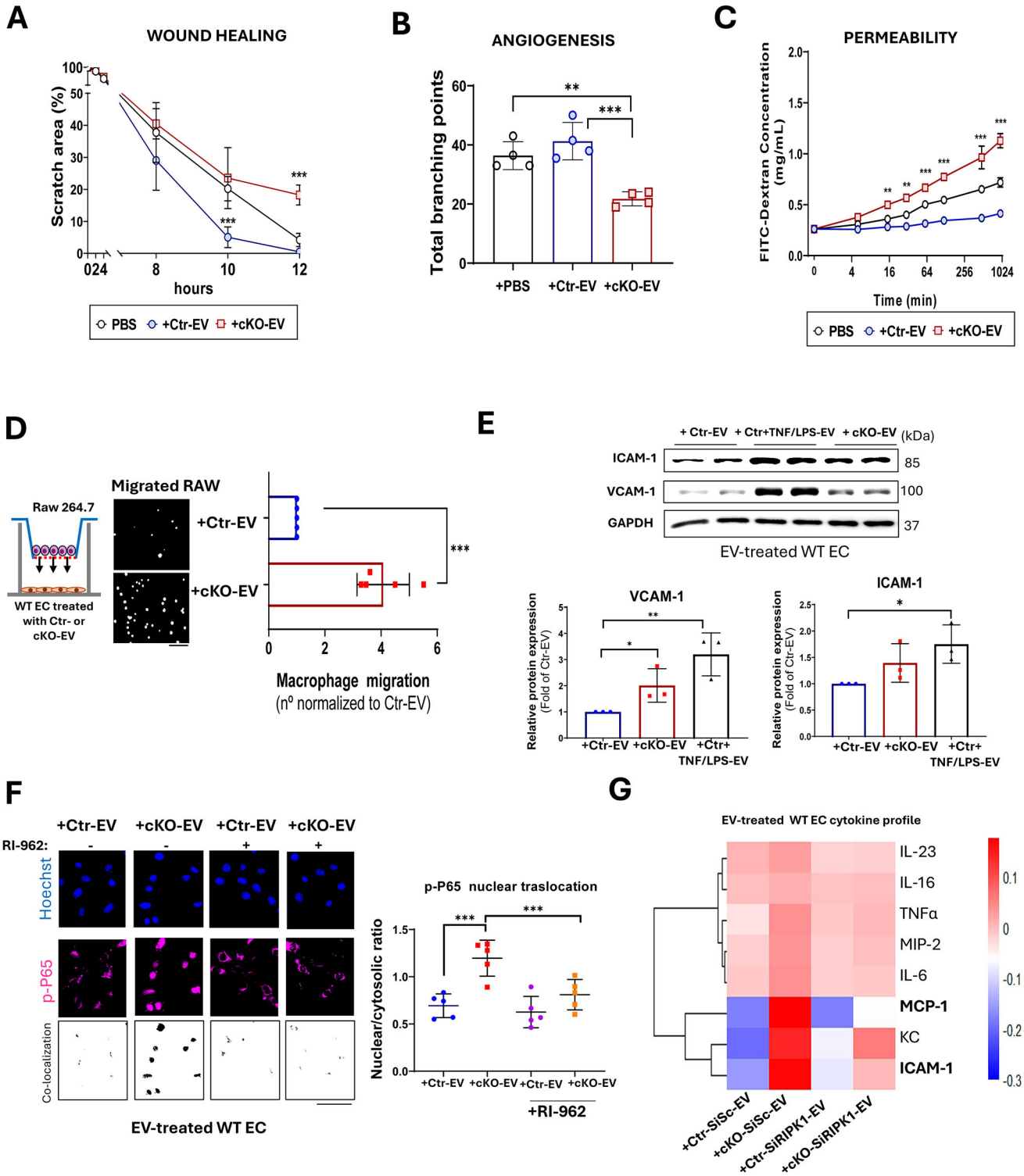

FIGURE 3 | Legend on next page.

expression was preserved in CT-EGFP mice but efficiently ablated in ecILK cKO-EGFP mice (Figure S6E).

Using this lineage-tracing system, we next assessed endothelial-derived circulating EVs. Flow cytometric quantification of EGFP-positive cEVs demonstrated a significant increase in endothelial-derived EVs in ecILK-cKO-EGFP mice compared with controls (Figure 4G). Moreover, circulating EVs from ecILK-cKO-EGFP mice were efficiently internalized by endothelial cells and showed greater uptake compared with EVs from control-EGFP mice (Figure S6F). Importantly, this analysis clarified that the apparent reduction in CD31+ vesicles observed in ecILK-cKO mice reflects a loss and redistribution of CD31 surface expression within the EV population rather than a decrease in endothelial EV release.

20013078, 2026, 6, Downloaded from https://isevjournals.onlinelibrary.wiley.com/doi/10.1002/jev2.70335 by Spanish Cochrane National Provision (Ministerio de Sanidad), Wiley Online Library on [31/07/2026]. See the Terms and Conditions (https://onlinelibrary.wiley.com/terms-and-conditions) on Wiley Online Library for rules of use; OA articles are governed by the applicable Creative Commons License

Finally, flow cytometry analysis showed that EGFP-positive circulating EVs from ecILK-cKO-EGFP mice were enriched in RIPK1, confirming that endothelial ILK deficiency promotes the release of circulating EVs carrying RIPK1 (Figures 4H and S6G).

Collectively, these results demonstrate that endothelial ILK loss profoundly reshapes the circulating EV landscape by increasing EV abundance, reprogramming surface marker composition (including CD31 redistribution), and promoting a shift toward a pro-inflammatory, endothelial-activation–associated molecular cargo characterized by metabolic stress signatures and selective enrichment of RIPK1.

3.5 | Exposure to Endothelial ILK-Deficient Circulating EVs Induces Systemic Vascular Inflammation and Cardiac Remodelling in Wild-Type Mice

To determine whether circulating EVs (cEVs) from endothelial ILK-deficient mice can induce vascular pathology, wild-type C57BL/6 mice were treated for 1 to 3 weeks with cEVs isolated from either control ILK-expressing mice (cEV^{CT}) or endothelial ILK-deficient mice ($cEV^{ecILK\text{-}cKO}$) (Figure 5A). Cardiac function and vascular structure were then evaluated.

Molecular analysis of coronary vessels revealed a rapid endothelial activation response as early as 1 week, characterized by increased expression of iNOS and ICAM-1 in endothelial cells (Figure 5B–D). These changes closely mirrored the inflammatory endothelial phenotype observed in ILK-deficient mice. At this stage, perivascular immune activation was already detectable, with increased accumulation of $CD68^+$ macrophages exhibiting a $CD86^+$ (M1-like) pro-inflammatory phenotype (Figure 55B,E,F). Full confocal datasets are shown in Figure S7A–C, respectively.

Sustained exposure to cEV resulted in progressive cardiac deterioration. By 3 weeks, treated mice displayed a significant reduction in left ventricular ejection fraction (LVEF) compared with cEV^{CT} controls (Figure S7D), together with impaired systolic performance reflected by altered Left Ventricular Internal Diameter diastolic to systolic ratio (LVIDd/LVIDs) (Figure S7E). In parallel, cardiac hypertrophy was evident, as indicated by an increased heart weight-to-tibial length ratio (Figure S7F).

Histological analysis confirmed extensive structural remodelling. Sirius Red staining revealed marked interstitial and perivascular collagen deposition, indicating pronounced myocardial fibrosis in $cEV^{ecILK\text{-}cKO}$-treated mice (Figure 5G).

Given the established role of endothelial ILK in maintaining vascular integrity (Reventun et al. 2023), microvascular architecture was assessed using Masson's trichrome staining. Exposure to $cEV^{ecILK\text{-}cKO}$ induced marked remodelling of small coronary vessels (10–60 μm), characterized by significant vascular wall thickening and enhanced perivascular collagen deposition (Figures 5H and S7G). These structural alterations closely paralleled the emergence of electrocardiographic abnormalities. Notably, within 1 week of $cEV^{ecILK\text{-}cKO}$ administration, approximately 40% of treated mice exhibited ischemia-like events, evidenced by ST-segment elevation on ECG, whereas no such abnormalities were detected in cEV^{CT}-treated controls. Both the incidence and severity of these events increased to a 70% after 3 weeks of exposure, recapitulating the phenotype observed in ecILK-cKO mice (Reventun et al. 2023).

Together, these findings strongly suggest that circulating EVs derived from an endothelial ILK-deficient background are sufficient to induce microvascular pathology.

3.6 | RIPK1-Enriched Circulating EVs Induce Early Endothelial Activation in Coronary and Aortic Vessels

To establish a cause–effect relationship and define the temporal sequence of vascular responses, wild-type mice were analysed at early time points (8 and 24 h) following cEV administration. At 8 h, $cEV^{ecILK\text{-}cKO}$ induced robust endothelial activation in coronary arteries, evidenced by increased endothelial RIPK1

FIGURE 3 | Proinflammatory EV from ILK deficient endothelial cells promote endothelial cell activation through RIPK-1. Recipient wild type endothelial cells were treated with extracellular vesicles (EVs) derived from ECs under the indicated conditions and different function parameters were studied. (A) Wound healing assay of EC treated with EV as indicated assessed using a scratch wound healing assay. EV were added at time 0 and Images were captured every 2 h until wound closure. Migration rates were quantified, $n = 4$ (per duplicate). (B) Endothelial tube formation was assessed during 8 h. Quantitative analysis of the total branching points normalized to PBS is shown, $n = 4$ per group. (C) Endothelial permeability assay: cells were treated with PBS, Ctr-and cKO-EV for 24 h. FITC-Dextran (150 kDa) permeability across EC monolayers was measured at the indicated time points. Data represent FITC-Dextran concentration (mg/mL) in the lower chamber ($n = 4$). (D) RAW 264.7 migration through transwell membranes to EC monolayers preciously exposed to Ctr- or cKO-EV for 8 h was analysed. A representative photograph of macrophages stained with Hoechst (white) adhering to the opposite side of the transwell membrane is shown. Scale bar = 50 μm, $n = 4$ (in duplicate). (E) Western blot analysis of ICAM-1 and VCAM expression in recipient wild-type EC treated with Ctr-EV, cKO-EV, or EV derived from Ctr-EC stimulated with TNF-α/LPS as a positive inflammatory signal ($n = 3$). (F) Representative immunofluorescence of p-P65 (magenta) nuclear translocation in wild-type endothelial cells treated with Ctr-V or cKO-EV, in the presence or the absence of the RIPK1 inhibitor RI-962; nuclei were stained with Hoechst (blue). The colocalization panel shows reduced phospho-P65 nuclear localization compared with cells treated with cKO-EVs. Scale bar = 10 μm. Quantification of p-P65 nuclear localization is shown ($n = 5$). (G) Heatmap showing cytokine profiles expression in recipient wild-type EC after treatment with extracellular vesicles. These EV were derived from either Si-Scramble (SiSc) or RIPK1silenced (SiRIPK1)-EC in the Ctr or cKO background (Ctr-or cKO-SiSc-EV and Ctr-or cKO-SiRIPK1-EV). Cytokines are colour-coded by expressions: red indicates upregulation, blue indicates downregulation, and white indicates no significant change. All values are presented as mean ± SD from at least three independent experiments. Statistical significance was determined using one-way ANOVA or Student's *t*-test, as appropriate; $^*p < 0.05$, $^{**}p < 0.01$, $^{***}p < 0.001$.

20013078, 2026, 6, Downloaded from https://isevjournals.onlinelibrary.wiley.com/doi/10.1002/jev2.70335 by Spanish Cochrane National Provision (Ministerio de Sanidad), Wiley Online Library on [31/07/2026]. See the Terms and Conditions (https://onlinelibrary.wiley.com/terms-and-conditions) on Wiley Online Library for rules of use; OA articles are governed by the applicable Creative Commons License

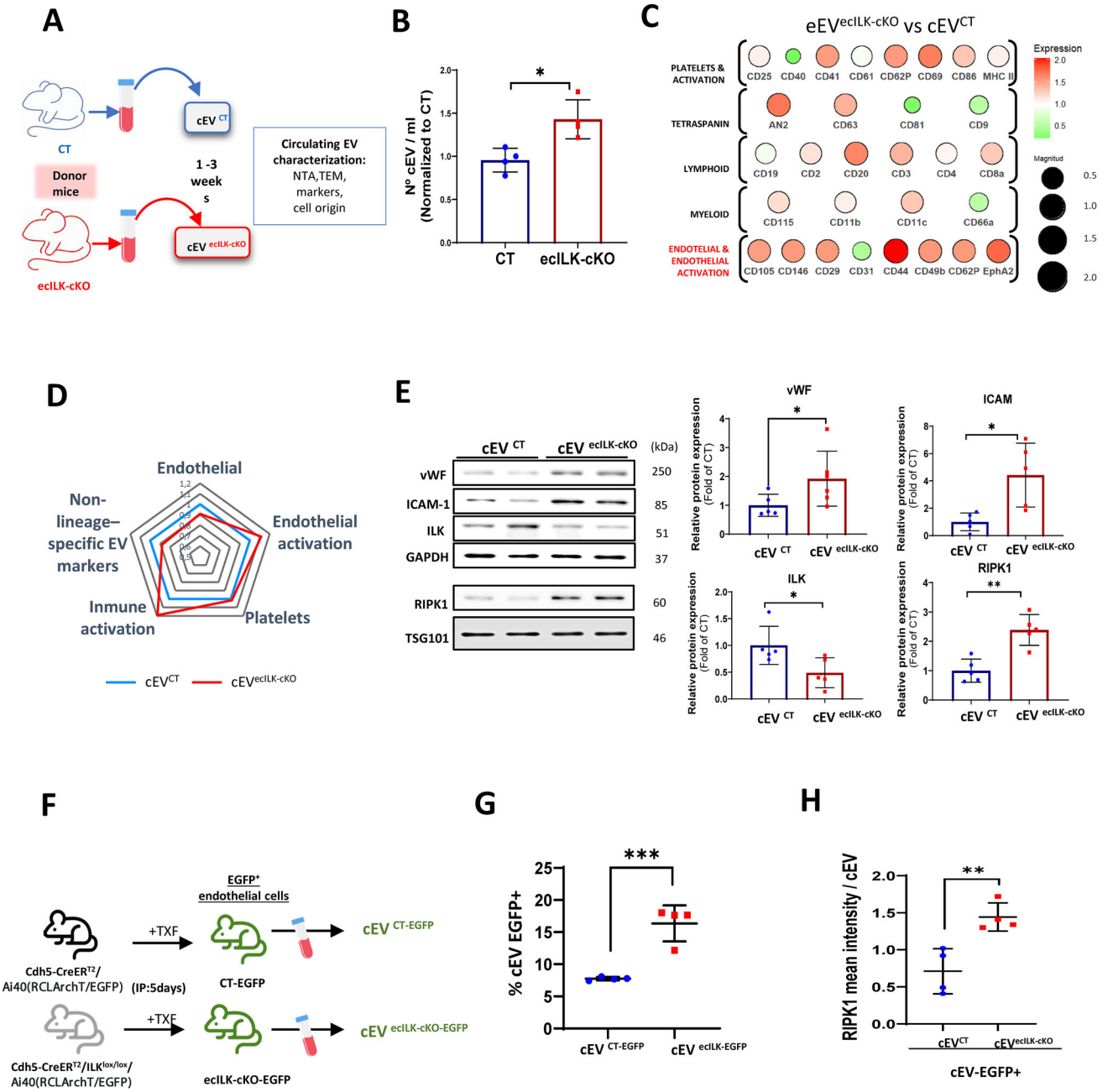

FIGURE 4 | Characterization of circulating extracellular vesicles (cEV) from control CT and ecILK-cKO mice. (A) Schematic representation of the workflow in vivo. EV from plasma were collected during the first and third week and characterized. (B) Concentration of cEV released per mL of plasma in CT and ecILK-cKO mice. (C) Expression profiles of cell-origin surface markers in circulating EVs isolated from CT and ecILK-cKO mice. Marker levels were quantified using a circulating EV surface-marker profiling kit ($n = 6$ per group). A strong upregulation of endothelial cell origin and endothelial activation markers is shown. (D) Radar plot summarizing the relative abundance of major EV surface marker categories detected. Values represent normalized signal intensities for each marker category. (E) Immunoblot analysis of vWF, ICAM-1 and ILK in circulating EVs isolated from CCT and ecILK-cKO mice ($n = 6$); the corresponding densitometric quantifications are shown on the right ($n = 5$). (F) Schematic representation of the genotype-dependent reporter activation in Ai40 (RCL-ArchT/EGFP) mice. Ai40 mice were crossed with mice carrying endothelial conditional ILK deletion or with their parental Cre line, in which Cre is activated in endothelial cells only in the presence of TXF. When given tamoxifen IP for 5 days, CT-EGFP mice will express EGFP fluorescence in endothelial cells, maintaining ILK expression intact, and ecILK-cKO mice will express EGFP and no endothelial ILK. (G) Flow cytometry quantification of cEV-eGFP+ populations in plasma from CT-EGFP and ecILK-cKO-EGFP mice ($n = 4$). (H) Flow cytometry analysis showing RIPK1 mean intensity in eGFP$^+$ cEVs isolated from CT-eGFP and ecILK-cKO-eGFP mice ($n = 4$). Statistical significance was determined using Student's *t*-test; $^*p < 0.05$, $^{**}p < 0.01$, $^{***}p < 0.001$.

20013078, 2026, 6, Downloaded from https://isevjournals.onlinelibrary.wiley.com/doi/10.1002/jev2.70335 by Spanish Cochrane National Provision (Ministerio de Sanidad), Wiley Online Library on [31/07/2026]. See the Terms and Conditions (https://onlinelibrary.wiley.com/terms-and-conditions) on Wiley Online Library for rules of use; OA articles are governed by the applicable Creative Commons License

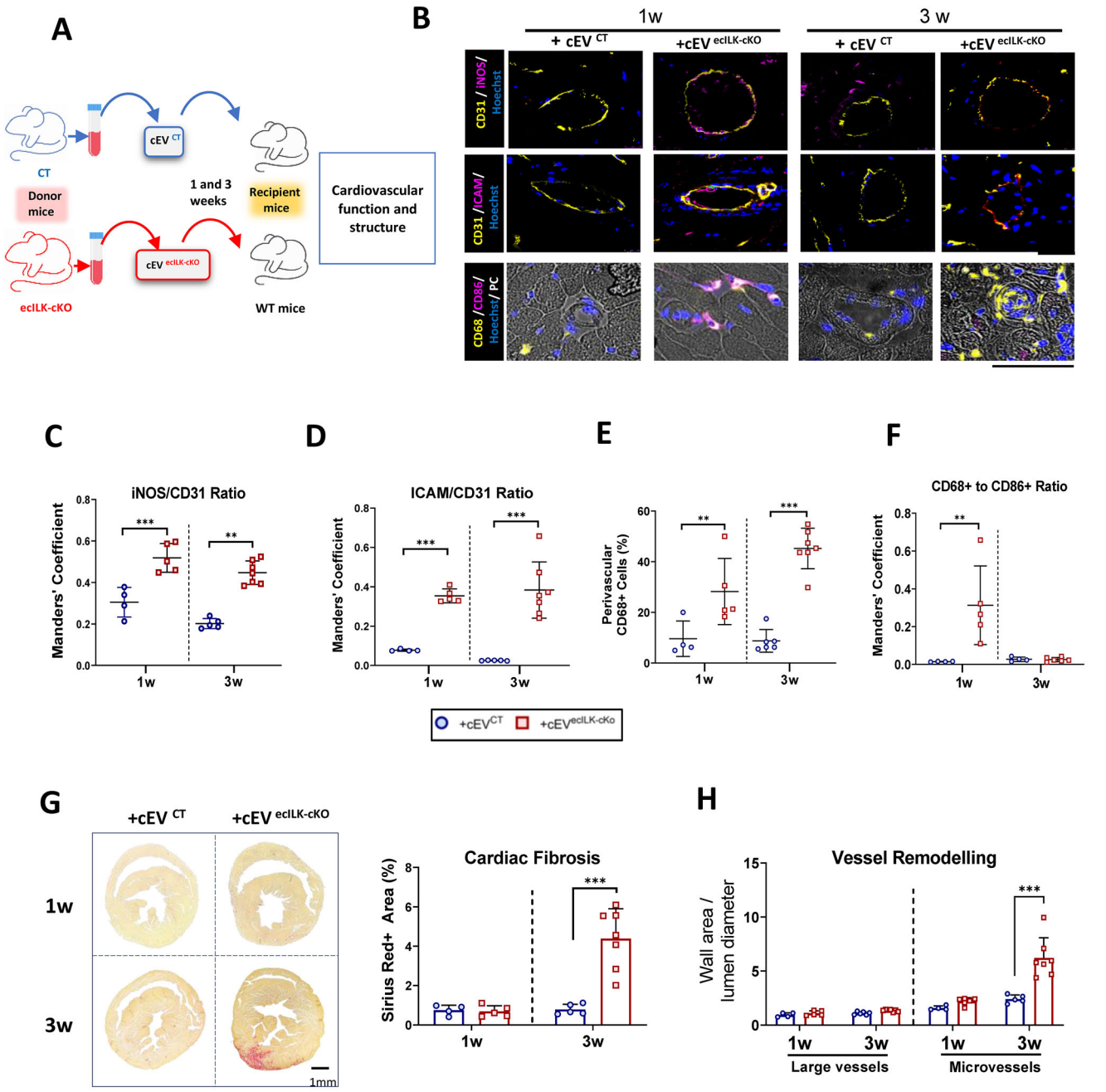

FIGURE 5 | cEV derived from ILK deficient mice propagate an inflammatory phenotype and induced cardiac dysfunction in wild- type mice. (A) Schematic representation of cEV transfer for the study of cardiovascular structure and function workflow. Recipient Wild-type mice were treated every 48 h for 1 and 3 weeks with cEV isolated from CT mice (cEV^{CT}) and ecILK-cKO mice ($cEV^{ecILK\text{-}cKO}$) in a timely fashion. PBS was used as negative control. Cardiac function and structural studies were conducted in recipient WT mice at 1 and 3 weeks. (B) Representative immunofluorescence analysis of cardiac tissue illustrating endothelial inflammatory activation. Upper panels show staining for the acute inflammatory marker iNOS (magenta) while middle panels show staining for the endothelial activation marker ICAM-1 (magenta), both colocalized with endothelial cells ($CD31^+$, yellow) and nuclei in blue in cEV ^{CT} and cEV $^{ecILK\text{-}cKO}$ at 1 and 3 weeks. Lower panels show immunofluorescence of perivascular regions, depicting macrophage infiltration ($CD68^+$, yellow) and polarization toward a pro-inflammatory M1 phenotype ($CD86^+$, magenta) under the same conditions as above. Phase-contrast (PC) microscopy (grey) was used to visualize vascular structures. Scale bar = 20 μm. Quantification of $CD31^+$ cells expressing (C) iNOS or (D) ICAM-1. (E) CD68+ Perivascular macrophage infiltration ($CD68^+$ cells within 10–20 μm of vessel wall). (F) CD68+/CD86+ ratio indicating M1 polarization. (G) Representative images of Sirius Red-stained cardiac tissue sections $+cEV^{CT}$, and $+cEV^{ecILK\text{-}cKO}$ groups at 1 and 3 weeks. Scale bar = 1 mm. Quantification of Sirius Red–positive area (fibrosis) relative to total cardiac tissue area under the conditions shown in (A). (H) Quantification of vascular remodelling in cardiac tissue under the same conditions as in (A), expressed as arteriolar wall area-to lumen area ratio. Vascular remodelling was significantly increased in WT mice treated for 3-weeks with $cEV^{ecILK\text{-}cKO}$ only in small vessels (10–60 mm) and remained unchanged in large vessels (>100 mm). For all analyses, data are presented as mean ± SD, with at least three randomly selected cardiac regions analysed per mouse across ventricular sections. Values represent the mean ± SD per animal. Statistical significance was determined using Student's *t*-test; $^*p < 0.05$, $^{**}p < 0.01$, $^{***}p < 0.001$.

20013078, 2026, 6, Downloaded from https://isevjournals.onlinelibrary.wiley.com/doi/10.1002/jev2.70335 by Spanish Cochrane National Provision (Ministerio de Sanidad), Wiley Online Library on [31/07/2026]. See the Terms and Conditions (https://onlinelibrary.wiley.com/terms-and-conditions) on Wiley Online Library for rules of use; OA articles are governed by the applicable Creative Commons License

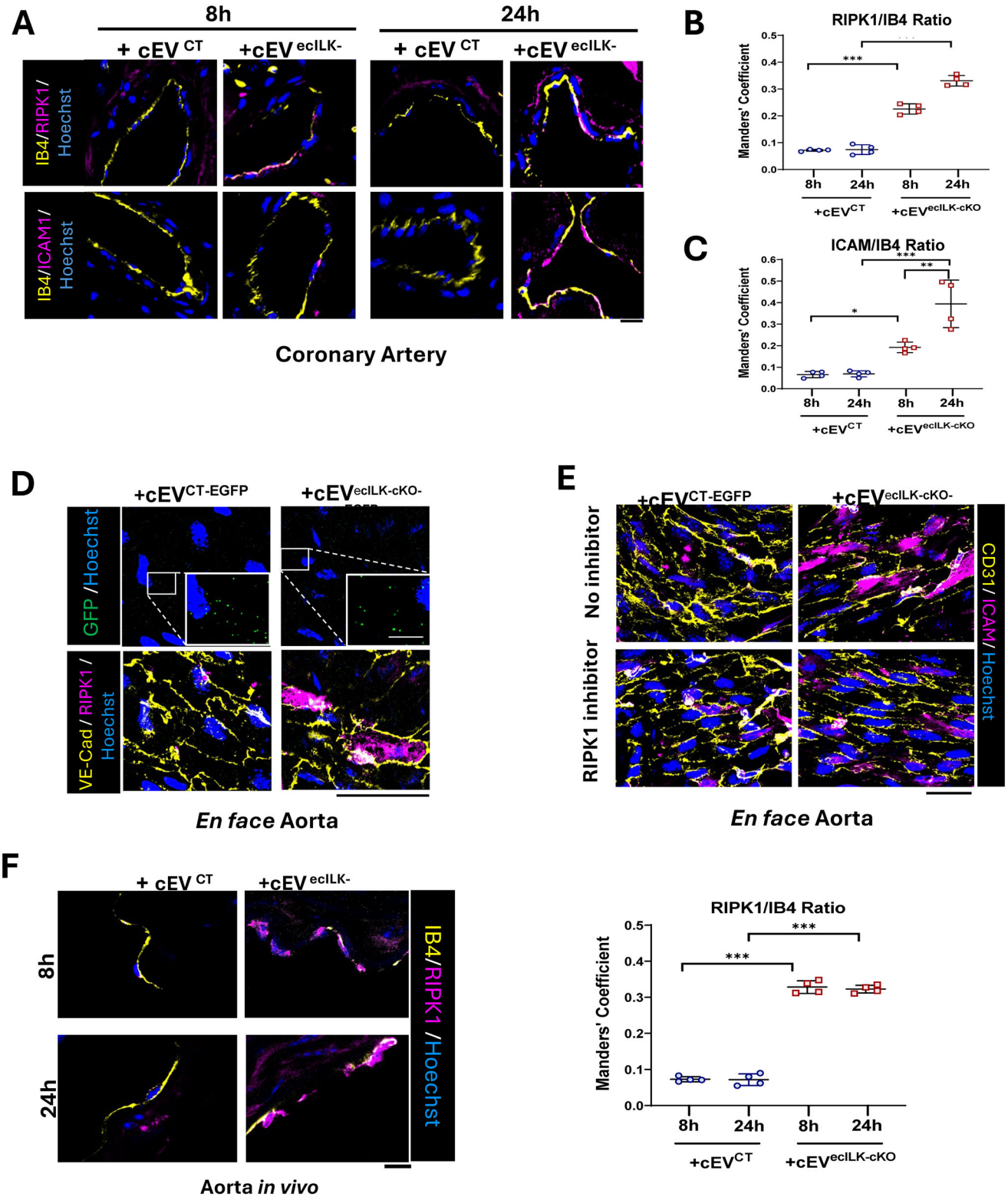

FIGURE 6 | Legend on next page.

expression and moderate upregulation of ICAM-1, in the absence of leukocyte infiltration (Figures 6A–C and S8A,B). By 24 h, this response progressed to a clear inflammatory phase characterized by significant CD68$^+$ macrophage recruitment to the perivascular space, indicating that immune cell infiltration follows initial endothelial activation (Figure S8C).

Next, to determine whether cEVs also affect distant vascular beds, aortic rings from wild-type mice were exposed ex vivo to the cEV generated in the EGFP reporter mice. cEV$^{ecILK\text{-}cKO\text{-}EGFP}$ induced a marked increase in endothelial RIPK1 and ICAM-1 expression in VE-Cadherin$^+$ endothelial cells, confirming direct endothelial activation across vascular territories (Figures 6D and

20013078, 2026, 6, Downloaded from https://isevjournals.onlinelibrary.wiley.com/doi/10.1002/jev2.70335 by Spanish Cochrane National Provision (Ministerio de Sanidad), Wiley Online Library on [31/07/2026]. See the Terms and Conditions (https://onlinelibrary.wiley.com/terms-and-conditions) on Wiley Online Library for rules of use; OA articles are governed by the applicable Creative Commons License

S8D). EV uptake was verified by detection of EGFP signal within endothelial cells (upper panel).

Pre-treatment with the RIPK1 inhibitor RI-962 significantly reduced ICAM-1 expression induced by cEV$^{ecILK\text{-}cKO\text{-}EGFP}$ (Figures 6E and S8E), indicating that endothelial activation by EVs depends on RIPK1-mediated signalling. In vivo, aortic RIPK1 induction was also detectable within 24 h of cEV administration (Figure 6F), confirming systemic vascular responsiveness.

Collectively, these data demonstrate that circulating EVs derived from ILK-deficient endothelial cells are sufficient to initiate a cascade of vascular events characterized by early endothelial activation, subsequent immune cell recruitment, progressive microvascular remodelling and ultimately cardiac dysfunction. Mechanistically, this process is at least in part mediated by RIPK1-dependent signalling and propagates across multiple vascular beds, including coronary arteries and the aorta, establishing a systemic pro-inflammatory vascular state.

3.7 | RIPK1 Mediates EV-Driven Endothelial Activation in Experimental and Human Atherosclerosis

To elucidate the translational significance of the ILK–EV–RIPK1 axis identified in endothelial ILK-deficient mice for vascular pathology, we initially examined its involvement in an experimental model of atherosclerosis. Consistent with reports of decreased endothelial ILK expression during plaque progression (Herranz et al. 2012, Reventun et al. 2017) and heightened RIPK1 signalling within atherosclerotic lesions (Karunakaran et al. 2021), ApoE knockout mice fed a high-fat diet for 16 weeks demonstrated substantially increased aortic RIPK1 expression relative to chow-fed controls, concomitant with reduced ILK levels in the endothelial layer (Figure 7A).

Circulating EVs isolated from atherosclerotic ApoE$^{-/-}$ mice displayed a molecular signature characterized by increased ICAM-1 and RIPK1 expression, together with reduced ILK levels (Figure 7B). Functionally, these EVs induced a robust inflammatory response in cultured endothelial cells, which was significantly attenuated by pharmacological inhibition of RIPK1. This RIPK1-dependent response mirrored that elicited by EVs derived from ecILK-cKO mice, indicating convergence on a shared signalling mechanism across experimental models.

We next evaluated whether this EV signature is also present in human coronary artery atherosclerosis (CA). Plasma-derived EVs from patients with CA exhibited a total EV load comparable to matched healthy controls (Figure 7D). Although the proportion of endothelial-derived (VE-cadherin^{+}) EVs was not significantly altered, CA-associated EVs were markedly enriched in RIPK1 (Figures 7E,F and S8F) Importantly, this enrichment was independent of body mass index (BMI), as no correlation between BMI and RIPK1 levels in endothelial EVs was observed (Figure S8G).

Functionally, EVs isolated from patients with CA induced a strong inflammatory activation in human coronary artery endothelial cells (CAEC), characterized by upregulation of ICAM-1-1 and RIPK1. This response was significantly reduced by RIPK1 inhibition (Figure 7G), confirming that RIPK1 activity is required for EV-induced endothelial activation in human disease.

Together, these findings identify RIPK1 as a central effector of EV-mediated endothelial activation in both endothelial ILK-deficient mice and atherosclerosis. This mechanism is conserved across experimental models and human coronary artery disease, supporting a unified pathway in which circulating EVs propagate vascular inflammation through RIPK1-dependent signalling.

4 | Discussion

The present study identifies endothelial ILK as a critical regulator of EV-mediated vascular communication. We demonstrate that loss of ILK drives the release of EVs enriched in pro-inflammatory mediators, most notably receptor-interacting protein kinase 1 (RIPK1), which propagate endothelial activation, microvascular inflammation, and cardiac dysfunction across vascular beds through RIPK1-dependent signalling. These findings establish a mechanistic link between endothelial ILK deficiency, EV cargo remodelling, and cardiovascular pathology, and define a conserved pathogenic axis that is operative in both experimental models and human coronary artery atherosclerosis. By showing that endothelial stress states reshape EV composition and bioactivity toward a pro-inflammatory phenotype, our work expands current understanding of EV-driven intercellular signalling and

FIGURE 6 | cEVs from ecILK-cKO mice promote early endothelial activation. (A) In vivo analysis of coronary endothelial expression of the activation markers RIPK1(upper panel) and ICAM-1 (lower panel) at 8 and 24 h after cEV injection. Representative immunofluorescence images of ICAM-1 or RIPK1 staining (magenta) in endothelial cells marked with IB4 (yellow). Nuclei were counterstained with Hoechst (blue). Multiple fields were analysed across at least three independent cardiac sections. Scale bar = 20 μm. The RIPK1 or ICAM to IB4+ endothelial cells ratio is shown on (B) and (C) ($n = 4$). (D) Aortic rings from WT mice were incubated ex vivo at 37°C for 24 h with cEV from CT-EGFP and ecILK-cKO-EGFP mice. *En face* staining of RIPK1 was performed. Representative immunofluorescence images of RIPK1(magenta) in endothelial cells (VE-Cadh, yellow) and EV-eGFP fluorescence (green) in the amplification (white square), indicating endothelial cell EV intake (Scale bar = 2 μm). Nuclei were counterstained with Hoechst (blue). Scale bar = 20 μm. Each experiment was repeated at least three times, with multiple aortic fragments analysed. (E) *En face* staining of ICAM-1 was performed as in D, but aorta fragments were pretreated (or not) with the RIPK1 inhibitor (RI-962). Representative immunofluorescence images of ICAM-1 staining (magenta) in endothelial cells (CD31^{+}; yellow) are displayed. Nuclei were counterstained with Hoechst in blue. Each experiment was repeated at least three times, with multiple aortic fragments analysed. Scale bar = 20 μm. (F) In vivo analysis of aortic endothelial expression of RIPK1 (magenta) at 8 and 24 h after cEV injection. Endothelial cells were marked with IB4 (yellow). Nuclei were counterstained with Hoechst (blue). Multiple fields were analysed across at least three independent aortic sections. Scale bar = 20 μm. The RIPK1 to IB4+ endothelial cells ratio is shown on the right ($n = 4$). Statistical significance was determined using one-way ANOVA; *$p < 0.05$, **$p < 0.01$, ***$p < 0.001$.

20013078, 2026, 6, Downloaded from https://isevjournals.onlinelibrary.wiley.com/doi/10.1002/jev2.70335 by Spanish Cochrane National Provision (Ministerio de Sanidad), Wiley Online Library on [31/07/2026]. See the Terms and Conditions (https://onlinelibrary.wiley.com/terms-and-conditions) on Wiley Online Library for rules of use; OA articles are governed by the applicable Creative Commons License

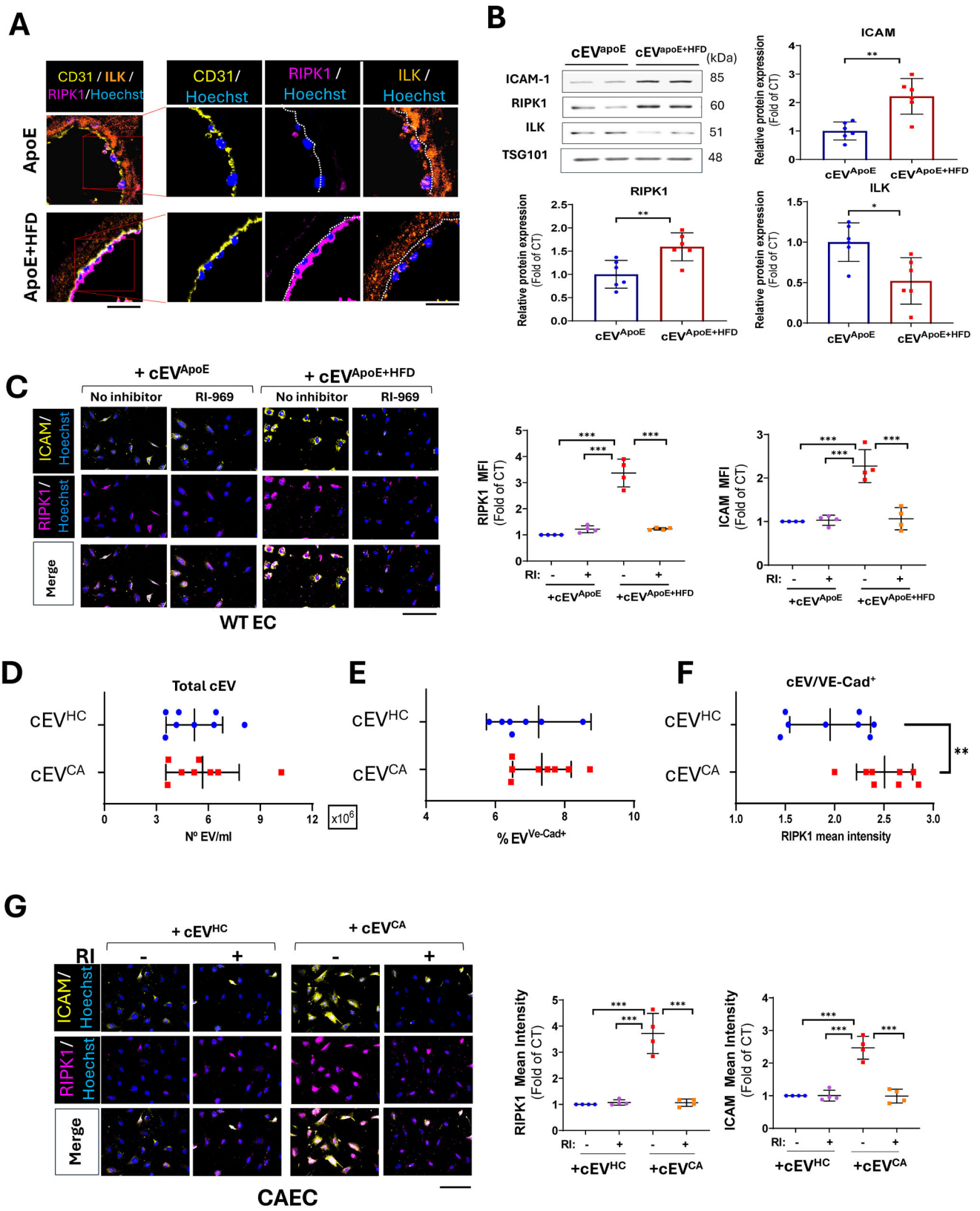

FIGURE 7 | Legend on next page.

20013078, 2026, 6, Downloaded from https://isevjournals.onlinelibrary.wiley.com/doi/10.1002/jev2.70335 by Spanish Cochrane National Provision (Ministerio de Sanidad), Wiley Online Library on [31/07/2026]. See the Terms and Conditions (https://onlinelibrary.wiley.com/terms-and-conditions) on Wiley Online Library for rules of use; OA articles are governed by the applicable Creative Commons License

positions RIPK1-enriched EVs as key mediators of vascular inflammation and dysfunction.

Endothelial activation, characterized by NF-kB signalling, VCAM-1, ICAM-1, and chemokine expression, as well as increased permeability, is a typical response to inflammatory, metabolic and mechanical stress (Welsh et al. 2020, Deanfield et al. 2007). Here, endothelial ILK depletion consistently elicited this activated phenotype, supporting a key role for ILK in maintaining endothelial homeostasis. ILK is a crucial hub in integrin-mediated signalling, modulating cytoskeletal dynamics, cellular adhesion and survival (Ansari et al. 2021, Delgado-Marin et al. 2024, Sánchez-Esteban et al. 2022). Mechanistically, ILK loss increased oxidative stress and promoted NF-kB activation, aligning with previous reports linking integrin signalling to redox imbalance and inflammatory gene expression (Reventun et al. 2017). The oxidative and nitrosative stress triggered by ILK deletion can explain these results. In the absence of ILK, eNOS becomes uncoupled, releasing superoxide; excessive ROS can induce NF-κB activity (Liu et al. 2023). Additionally, ROS can activate the PI3K pathway, which, in turn, phosphorylates AKT, thereby activating NF-κB (Kma and Baruah 2022, Cho et al. 2016).

A significant contribution of this study is the demonstration that decreased ILK expression profoundly alters the cargo and biological effects of endothelial EV. EV derived from ILK-deficient endothelial cells (cKO-EV) contained proinflammatory molecules that could amplify immune cell recruitment and perpetuate the inflammatory milieu. These results align with prior studies demonstrating the role of EV in transmitting inflammatory signals during atherosclerosis and myocardial infarction (Ge et al. 2021). Moreover, these EVs exhibited a distinct zeta potential, suggesting changes in surface composition and protein corona that may enhance their interaction with recipient cells (Feng et al. 2021, Williams et al. 2019). Functionally, whereas EV released from control cells preserved angiogenesis and endothelial repair, cKO-EV impaired endothelial proliferation, migration and network formation. This dichotomy highlights the plasticity of endothelial EV under stress and reinforces emerging concepts that EV from healthy endothelium is reparative, whereas EV released under pathological conditions acquire deleterious properties (Choi et al. 2023).

Proteomic and pathway analyses further revealed that cKO-EVs were enriched in inflammatory, glycolytic and hypoxia-associated pathways, signatures consistent with metabolic reprogramming typical of activated endothelium (Liu et al. 2023, Han et al. 2022). Conversely, complement-related pathways were reduced, suggesting dysregulated immune-modulatory functions, as reported in EVs from inflammatory and vascular conditions (Yoshida and Nishi 2022). Altogether, these findings indicate that ILK deficiency induces a defined inflammatory EV phenotype with potential functional consequences for the vascular microenvironment.

One of the most striking findings was the presence of RIPK1 in cKO-EV. RIPK1 is a central regulator of inflammatory and cell-death pathways (Moriwaki et al. 2022, Orozco et al. 2014, Riebeling et al. 2021). Recent studies have identified its role in various CVD, including atherosclerosis (Karunakaran et al. 2021), myocardial infarction (Oerlemans et al. 2012, Sun et al. 2024), graft arteriosclerosis (Lu et al. 2023) and aortic dissecting aneurysm (Wang et al. 2017). Post-translational modifications tightly regulate RIPK1 activity. When polyubiquitinated, RIPK1 acts as a scaffold that stabilizes the IKKα/β complex, promoting IκBα degradation, nuclear translocation of NF-κB, and transcription of genes involved in inflammation and survival. Interestingly, RIPK1 had not previously been identified as an EV cargo, but several studies have shown that necroptotic or inflammatory signalling can promote the release of EVs that contain components of the necrosome, including RIPK3 and MLKL (Gupta et al. 2022, Shlomovitz et al. 2021). Such EV can activate immune cells and promote the secretion of pro-inflammatory cytokines (Baxter 2020). Moreover, the essential role of RIPK1 kinase activity in endothelial injury and vascular inflammation in vivo underscores the relevance of RIPK1-driven pathways in vascular pathology (Karunakaran et al. 2021). Consistent with these reports, we show that ILK-deficient EC exhibit increased RIPK1 expression. In addition, not only do KO-EV carry RIPK1, but also RIPK-enriched EV can activate RIPK1-dependent signalling in recipient endothelial cells, as demonstrated using the RIPK1 inhibitor (previously shown to suppress inflammation in vivo) (Li et al. 2022). The lack of effect of the EV from RIPK1-silenced endothelial cells suggests a mechanism of horizontal transfer of inflammatory potential. Although the precise mechanism linking ILK loss to RIPK1 incorporation into EVs remains undefined, our data are consistent with a model in which ILK deficiency disrupts

FIGURE 7 | cEV from atherosclerotic mice and from patients with coronary atherosclerosis are enriched in RIPK1 and promote endothelial activation. (A) Representative immunofluorescence of aortic sections from ApoE$^{-/-}$ mice fed with regular (ApoE) or high-fat diet (ApoE+HFD) for 16 weeks, showing CD31 (yellow), ILK (orange) and RIPK1 (magenta) expression. Nuclei were counterstained with Hoechst (blue). Scale bar = 40 μm and 20 μm in the amplification. (B) Immunoblot analysis of ICAM-1, RIPK1 and ILK in cEV from ApoE and ApoE+HFD mice (cEV ^{ApoE} and cEV $^{ApoE+HFD}$, respectively) ($n = 6$). (C) Wild-type mouse aortic EC were treated with cEV ^{ApoE} and cEV $^{ApoE+HFD}$ in the presence or absence of RIPK1 inhibitor RI-962(RI). Immunofluorescence analysis of ICAM-1 (yellow) and RIPK1 (magenta) expression. Nuclei were counterstained with Hoechst (blue). Quantification of RIPK1 and ICAM mean intensities are shown on the right. Scale bar = 20 μm ($n = 4$). (D) Concentration of cEV released per mL of plasma in healthy controls individuals (cEV^{HC}) and coronary atherosclerosis patients (cEV^{CA}) ($n = 8$). (E) Flow cytometry quantification of VE-Cadherin+ cEV populations in plasma from healthy controls individuals and CA patients. Results are expressed in percentage from the Healthy Controls. (F) Flow cytometry analysis of RIPK1 enrichment in VE-Cadh+ cEV from healthy and CA patients. (G) Human coronary artery cells (CAEC) were treated with cEV derived from healthy controls and CA patients in the presence or absence of RIPK1 inhibitor RI-962(RI). Immunofluorescence analysis of ICAM-1 (yellow) and RIPK1 (magenta) expression is shown. Nuclei were counterstained with Hoechst (blue). Scale bar = 20 μm. Quantification of RIPK1 and ICAM mean intensities are shown on the right ($n = 4$). Results are presented as mean ± SD Statistical significance was determined using one-way ANOVA or Student's t-test, as appropriate; *$p < 0.05$, **$p < 0.01$, ***$p < 0.001$.
[Correction added on 4 July 2026, after first online publication: Figure 7 has been changed.]

20013078, 2026, 6, Downloaded from https://isevjournals.onlinelibrary.wiley.com/doi/10.1002/jev2.70335 by Spanish Cochrane National Provision (Ministerio de Sanidad), Wiley Online Library on [31/07/2026]. See the Terms and Conditions (https://onlinelibrary.wiley.com/terms-and-conditions) on Wiley Online Library for rules of use; OA articles are governed by the applicable Creative Commons License

integrin-dependent survival signals, leading to eNOS uncoupling (Herranz et al. 2012), and increased oxidative and nitrosative stress. This redox imbalance, together with sustained NF-κB activation, could create a transcriptional environment favourable to RIPK1 induction and its subsequent incorporation into EVs.

The translational relevance of RIPK1-positive EV was demonstrated in vivo. Circulating EV from ecILK-deficient mice induced endothelial activation, ischemic changes, cardiac macrophage infiltration, microvascular remodelling, fibrosis, and cardiac dysfunction in healthy recipients, phenocopying key features of ecILK-cKO mice (Reventun et al. 2023). Circulating EV profiling revealed that platelet-derived EV content, the dominant circulating population (Ferreira et al. 2020), did not differ significantly between control and endothelial ILK-deficient conditions. However, there was a notable increase in EVs carrying markers of activated endothelial cells and immune cells. This pattern indicates that endothelial ILK deficiency triggers a coordinated multicellular response, in which the dysfunctional endothelium both modifies its own EV release (quantity and/or cargo)[66], and promotes the activation of circulating immune cells that also shed EVs with distinct surface markers and inflammatory cargo, thereby contributing to the observed multicellular EV signature, which could amplify the initial signal originated in the ILK-deficient endothelium (Jansen et al. 2017). The in vivo EV transfer experiments further support these conclusions, defining a coherent temporal sequence of EV-associated vascular dysfunction, in which early endothelial signalling changes characterized by endothelial activation and RIPK1 upregulation, precede downstream inflammatory outcomes, including immune cell infiltration and macrophage recruitment. The predominance of microvascular alterations observed after chronic exposure to $cEV^{ecILK\text{-}cKO}$ indicates the sensitivity of the microvasculature to EV-mediated inflammatory signalling.

From a broader perspective, our findings fit within an expanding body of literature highlighting EVs as a central mediator of cardiovascular and systemic disease. EVs modulate angiogenesis, immune responses, endothelial activation and tissue repair in diverse contexts, including myocardial infarction, atherosclerosis, diabetes and cancer (Zhu et al. 2024, Huang et al. 2023, Yao et al. 2024, Suades et al. 2024, Prieto-Vila et al. 2024). We extend these observations by identifying ILK as a regulator of EV composition and by demonstrating that RIPK1-enriched EVs drive endothelial inflammation and tissue remodelling. Notably, similar EV signatures were identified in $ApoE^{-/-}$ mice fed a high-fat diet, which exhibit reduced endothelial ILK expression (Herranz et al. 2012), suggesting that RIPK1-positive EVs may represent a conserved pathogenic axis across CVD. Indeed, we show here that circulating EV from patients with coronary artery atherosclerosis carry RIPK1 and activate human coronary endothelial cells, further supporting their translational relevance and highlighting their potential as biomarkers or therapeutic targets.

This study has several limitations relevant to the EV field. Although endothelial markers (CD31 and VE-cadherin) and endothelial-restricted GFP reporter mice support a major contribution from endothelial-derived cEVs, the precise tissue source of the ILK-deficiency–associated EV signature could not be determined. In addition, circulating EVs showed markers of immune activation, but it remains unclear whether this reflects secondary immune responses driven by endothelial activation or a direct contribution from immune cells. Importantly, we cannot exclude the possibility that cEVs may also act on other organs, potentially contributing to systemic vascular complications. Finally, whether EVs from healthy endothelium could counteract ILK-dependent vascular changes remains unknown. Further studies are needed to clarify these mechanisms and the broader relevance of ILK-dependent endothelial EV signalling.

In conclusion, we identify ILK as a central regulator of endothelial activation and reveal that ILK deficiency induces the release of RIPK1-enriched EV with potent pro-inflammatory and pathogenic activity. These EVs propagate ED and cardiovascular remodelling signals, establishing a mechanistic connection between endothelial ILK loss and systemic cardiovascular pathology. Our findings open new avenues for exploring RIPK1-positive EV as biomarkers of endothelial stress and for targeting EV-mediated inflammatory signalling in cardiovascular disease.

Author Contributions

Cook-Calvete A.: investigation, writing – original draft, formal analysis, data curation, methodology, validation. **Delgado-Marín M.**: investigation, writing – original draft, methodology, validation, formal analysis, data curation. **Jorquera Ortega S.**: investigation. **Moreta S.**: investigation. **Castro-Pinto M.**: visualization, resources, investigation. **López-Menendez J.**: writing – review and editing, methodology. **Fernandez-Rodriguez B.**: investigation. **García-García J.**: investigation. **Zaragoza C.**: writing – review and editing, resources, supervision. **Saura M.**: conceptualization, funding acquisition, writing – review and editing, project administration, supervision, formal analysis, visualization, resources, validation.

Acknowledgements

We thank the members of the Tissue Culture Unit at Universidad de Alcalá for their assistance with confocal microscopy (NANBIOSIS-CIBER-BNN) and flow cytometry experiments. In addition, we thank the members of the Proteomic Unit at Malaga University (UMA) for their assistance with the proteomic study.

Funding

This research was funded by Instituto de Salud Carlos III (grant:PI23/01034, co-financed by the European Union); Junta de Comunidades de Castilla La Mancha (SBPLY/23/180225/000081) cofinanced through the ERDF and by the JCCM through INNOCAM, and Comunidad de Madrid, Biomedicine Activities Program (S2022/BMD-7223) (M. Saura). Grant "Generacion del conocimiento" PID2023-152919OB-100 funded by MICIU/AEI 10.13039/501100011033 and by "ERDF A way of making Europe", ERDF/EU (C. Zaragoza).

Conflicts of Interest

The authors declare no conflicts of interest.

Data Availability Statement

The data that support the findings of this study are available from the corresponding author upon reasonable request.

20013078, 2026, 6, Downloaded from https://isevjournals.onlinelibrary.wiley.com/doi/10.1002/jev2.70335 by Spanish Cochrane National Provision (Ministerio de Sanidad), Wiley Online Library on [31/07/2026]. See the Terms and Conditions (https://onlinelibrary.wiley.com/terms-and-conditions) on Wiley Online Library for rules of use; OA articles are governed by the applicable Creative Commons License

References

Amersfoort, J., G. Eelen, and P. Carmeliet. 2022. "Immunomodulation by Endothelial Cells—Partnering up With the Immune System?" *Nature Reviews Immunology* 22, no. 9: 576–588. https://doi.org/10.1038/s41577-022-00694-4.

Ansari, S. A., S. Keshava, U. R. Pendurthi, and L. V. M. Rao. 2021. "Oxidative Stress Product, 4-Hydroxy-2-Nonenal, Induces the Release of Tissue Factor-Positive Microvesicles From Perivascular Cells Into Circulation." *Arteriosclerosis, Thrombosis, and Vascular Biology* 41, no. 1: 250–265. https://doi.org/10.1161/ATVBAHA.120.315187.

Baxter, A. A. 2020. "Stoking the Fire: How Dying Cells Propagate Inflammatory Signalling Through Extracellular Vesicle Trafficking." *International Journal of Molecular Sciences* 21, no. 19: 7256. https://doi.org/10.3390/ijms21197256.

Bijnsdorp, I. V., A. A. Geldof, M. Lavaei, S. R. Piersma, R. J. A. van Moorselaar, and C. R. Jimenez. 2013. "Exosomal ITGA3 interferes With Non-Cancerous Prostate Cell Functions and is Increased in Urine Exosomes of Metastatic Prostate Cancer Patients." *Journal of Extracellular Vesicles* 2, no. 1: 22097. https://doi.org/10.3402/jev.v2i0.22097.

Cho, R. L., C. C. Yang, I. T. Lee, et al. 2016. "Lipopolysaccharide Induces ICAM-1 Expression via a c-Src/NADPH Oxidase/ROS-Dependent NF-κB Pathway in human Pulmonary Alveolar Epithelial Cells." *American Journal of Physiology-Lung Cellular and Molecular Physiology* 310, no. 7: L639–L657. https://doi.org/10.1152/ajplung.00109.2014.

Choi, Y. Y., A. Kim, Y. Lee, Y. H. Lee, et al. 2023. "The miR-126-5p and miR-212-3p in the Extracellular Vesicles Activate Monocytes in the Early Stage of Radiation-Induced Vascular Inflammation Implicated in Atherosclerosis." *Journal of Extracellular Vesicles* 12, no. 5: e12325. https://doi.org/10.1002/jev2.12325.

Deanfield, J. E., J. P. Halcox, and T. J. Rabelink. 2007. "Endothelial Function and Dysfunction." *Circulation* 115, no. 10: 1285–1295. https://doi.org/10.1161/CIRCULATIONAHA.106.652859.

Delgado-Marin, M., S. Sánchez-Esteban, A. Cook-Calvete, S. Jorquera-Ortega, C. Zaragoza, and M. Saura. 2024. "Indoxyl Sulfate-Induced Valve Endothelial Cell Endothelial-to-Mesenchymal Transition and Calcification in an Integrin-Linked Kinase-Dependent Manner." *Cells* 13, no. 6: 481. https://doi.org/10.3390/cells13060481.

Deshmane, S. L., S. Kremlev, S. Amini, and B. E. Sawaya. 2009. "Monocyte Chemoattractant Protein-1 (MCP-1): An Overview." *Journal of Interferon & Cytokine Research* 29, no. 6: 313–326. https://doi.org/10.1089/jir.2008.0027.

De Sousa, K. P., I. Rossi, M. Abdullahi, M. I. Ramirez, D. Stratton, and J. M. Inal. 2023. "Isolation and Characterization of Extracellular Vesicles and Future Directions in Diagnosis and Therapy." *WIREs Nanomedicine and Nanobiotechnology* 15, no. 1: e1835. https://doi.org/10.1002/wnan.1835.

Feng, K., X. Xie, J. Yuan, L. Gong, et al. 2021. "Reversing the Surface Charge of MSC-Derived Small Extracellular Vesicles by εPL-PEG-DSPE for Enhanced Osteoarthritis Treatment." *Journal of Extracellular Vesicles* 10, no. 13: e12160. https://doi.org/10.1002/jev2.12160.

Ferreira, P. M., E. Bozbas, S. D. Tannetta, N. Alroqaiba, et al. 2020. "Mode of Induction of Platelet-Derived Extracellular Vesicles Is a Critical Determinant of Their Phenotype and Function." *Scientific Reports* 10, no. 1: 18061. https://doi.org/10.1038/s41598-020-73005-3.

Ge, X., Q. Meng, L. Wei, J. Liu, et al. 2021. "Myocardial Ischemia-Reperfusion Induced Cardiac Extracellular Vesicles Harbour Proinflammatory Features and Aggravate Heart Injury." *Journal of Extracellular Vesicles* 10, no. 4: e12072. https://doi.org/10.1002/jev2.12072.

Górska, A., and A. J. Mazur. 2022. "Integrin-linked Kinase (ILK): The Known vs. the Unknown and Perspectives." *Cellular and Molecular Life Sciences* 79, no. 2: 100. https://doi.org/10.1007/s00018-021-04104-1.

Grange, C., and B. Bussolati. 2022. "Extracellular Vesicles in Kidney Disease." *Nature Reviews Nephrology* 18, no. 8: 499–513. https://doi.org/10.1038/s41581-022-00586-9.

Grashoff, C., A. Aszódi, T. Sakai, E. B. Hunziker, and R. Fässler. 2003. "Integrin-Linked Kinase Regulates Chondrocyte Shape and Proliferation." *EMBO Reports* 4, no. 4: 432–438. https://doi.org/10.1038/sj.embor.embor801.

Guo, J., C. Wu, X. Lin, J. Zhou, et al. 2021. "Establishment of a Simplified Dichotomic Size-Exclusion Chromatography for Isolating Extracellular Vesicles Toward Clinical Applications." *Journal of Extracellular Vesicles* 10, no. 11: e12145. https://doi.org/10.1002/jev2.12145.

Gupta, K., K. A. Brown, M. L. Hsieh, B. M. Hoover, et al. 2022. "Necroptosis is Associated With Rab27-Independent Expulsion of Extracellular Vesicles Containing RIPK3 and MLKL." *Journal of Extracellular Vesicles* 11, no. 9: e12261. https://doi.org/10.1002/jev2.12261.

Han, C., J. Yang, E. Zhang, Y. Jiang, et al. 2022. "Metabolic Labeling of Cardiomyocyte-Derived Small Extracellular-Vesicle (sEV) miRNAs Identifies miR-208a in Cardiac Regulation of Lung Gene Expression." *Journal of Extracellular Vesicles* 11, no. 10: e12246. https://doi.org/10.1002/jev2.12246.

Herranz, B., S. Marquez, B. Guijarro, E. Aracil, et al. 2012. "Integrin-Linked Kinase Regulates Vasomotor Function by Preventing Endothelial Nitric Oxide Synthase Uncoupling." *Circulation Research* 110, no. 3: 439–449. https://doi.org/10.1161/CIRCRESAHA.111.253948.

Hosseinkhani, B., S. Kuypers, N. M. S. van den Akker, D. G. M. Molin, and L. Michiels. 2018. "Extracellular Vesicles Work as a Functional Inflammatory Mediator Between Vascular Endothelial Cells and Immune Cells." *Frontiers in Immunology* 9: 1789. https://doi.org/10.3389/fimmu.2018.01789.

Huang, Q., Y. Sun, L. Peng, J. Sun, et al. 2023. "Extracellular Vesicle-Packaged ILK From Mesothelial Cells Promotes Fibroblast Activation in Peritoneal Fibrosis." *Journal of Extracellular Vesicles* 12, no. 7: e12334. https://doi.org/10.1002/jev2.12334.

Humphries, F., S. Yang, B. Wang, and P. N. Moynagh. 2015. "RIP Kinases: Key Decision Makers in Cell Death and Innate Immunity." *Cell Death & Differentiation* 22, no. 2: 225–236. https://doi.org/10.1038/cdd.2014.126.

Jain, S., H. Jariyal, A. Srivastava, and P. Sengupta. 2020. "Target Specific Intracellular Quantification of Etoposide by Quadrupole-time of Flight Based Mass Spectrometric Method." *Journal of Chromatography B* 1152: 122233. https://doi.org/10.1016/j.jchromb.2020.122233.

Jansen, F., Q. Li, A. Pfeifer, and N. Werner. 2017. "Endothelial- and Immune Cell-Derived Extracellular Vesicles in the Regulation of Cardiovascular Health and Disease." *JACC: Basic to Translational Science* 2, no. 6: 790–807. https://doi.org/10.1016/j.jacbts.2017.08.004.

Kadota, T., Y. Fujita, J. Araya, N. Watanabe, et al. 2021. "Human Bronchial Epithelial Cell-Derived Extracellular Vesicle Therapy for Pulmonary Fibrosis via Inhibition of TGF-β-WNT Crosstalk." *Journal of Extracellular Vesicles* 10, no. 10: e12124. https://doi.org/10.1002/jev2.12124.

Karunakaran, D., M. A. Nguyen, M. Geoffrion, D. Vreeken, et al. 2021. "RIPK1 Expression Associates With Inflammation in Early Atherosclerosis in Humans and Can Be Therapeutically Silenced to Reduce NF-κB Activation and Atherogenesis in Mice." *Circulation* 143, no. 2: 163–177. https://doi.org/10.1161/CIRCULATIONAHA.118.038379.

Kma, L., and T. J. Baruah. 2022. "The Interplay of ROS and the PI3K/Akt Pathway in Autophagy Regulation." *Biotechnology and Applied Biochemistry* 69, no. 1: 248–264. https://doi.org/10.1002/bab.2104.

Knöll, R., R. Postel, J. Wang, R. Krätzner, et al. 2007. "Laminin-α4 and Integrin-Linked Kinase Mutations Cause Human Cardiomyopathy via Simultaneous Defects in Cardiomyocytes and Endothelial Cells." *Circulation* 116, no. 5: 515–525. https://doi.org/10.1161/CIRCULATIONAHA.107.689984.

Koliha, N., Y. Wiencek, U. Heider, C. Jüngst, et al. 2016. "A Novel Multiplex Bead-Based Platform Highlights the Diversity of Extracellular Vesicles." *Journal of Extracellular Vesicles* 5, no. 1: 29975. https://doi.org/10.3402/jev.v5.29975.

Kusumbe, A. P., S. K. Ramasamy, and R. H. Adams. 2014. "Coupling of Angiogenesis and Osteogenesis by a Specific Vessel Subtype in

20013078, 2026, 6, Downloaded from https://isevjournals.onlinelibrary.wiley.com/doi/10.1002/jev2.70335 by Spanish Cochrane National Provision (Ministerio de Sanidad), Wiley Online Library on [31/07/2026]. See the Terms and Conditions (https://onlinelibrary.wiley.com/terms-and-conditions) on Wiley Online Library for rules of use; OA articles are governed by the applicable Creative Commons License

Bone." *Nature* 507, no. 7492: 323–328. https://doi.org/10.1038/nature13145.

Lee, K. S., J. Lee, H. K. Kim, S. H. Yeom, et al. 2021. "Extracellular Vesicles From Adipose Tissue-Derived Stem Cells Alleviate Osteoporosis Through Osteoprotegerin and miR-21-5p." *Journal of Extracellular Vesicles* 10, no. 12: e12152. https://doi.org/10.1002/jev2.12152.

Li, Y., L. Zhang, Y. Wang, J. Zou, et al. 2022. "Generative Deep Learning Enables the Discovery of a Potent and Selective RIPK1 Inhibitor." *Nature Communications* 13, no. 1: 6891. https://doi.org/10.1038/s41467-022-34692-w.

Liangsupree, T., E. Multia, and M. L. Riekkola. 2021. "Modern Isolation and Separation Techniques for Extracellular Vesicles." *Journal of Chromatography A* 1636: 461773. https://doi.org/10.1016/j.chroma.2020.461773.

Liberzon, A., C. Birger, H. Thorvaldsdóttir, M. Ghandi, J. P. Mesirov, and P. Tamayo. 2015. "The Molecular Signatures Database Hallmark Gene Set Collection." *Cell Systems* 1, no. 6: 417–425. https://doi.org/10.1016/j.cels.2015.12.004.

Liu, A., P. Luo, and H. Huang. 2023. "New Insight of Complement System in the Process of Vascular Calcification." *Journal of Cellular and Molecular Medicine* 27, no. 9: 1168–1178. https://doi.org/10.1111/jcmm.17732.

Liu, J., X. Han, T. Zhang, K. Tian, Z. Li, and F. Luo. 2023. "Reactive Oxygen Species (ROS) Scavenging Biomaterials for Anti-inflammatory Diseases: From Mechanism to Therapy." *Journal of Hematology & Oncology* 16, no. 1: 116. https://doi.org/10.1186/s13045-023-01512-7.

Loyer, X., I. Zlatanova, C. Devue, M. Yin, et al. 2018. "Intra-Cardiac Release of Extracellular Vesicles Shapes Inflammation Following Myocardial Infarction." *Circulation Research* 123, no. 1: 100–106. https://doi.org/10.1161/CIRCRESAHA.117.311326.

Lu, W., J. Xie, R. Gu, and B. Xu. 2017. "Expression of Integrin-Linked Kinase Improves Cardiac Function in a Swine Model of Myocardial Infarction." *Experimental and Therapeutic Medicine* 13, no. 5: 1868–1874. https://doi.org/10.3892/etm.2017.4162.

Lu, Y., Y. Leng, Y. Li, J. Wang, et al. 2023. "Endothelial RIPK1 Protects Artery Bypass Graft against Arteriosclerosis by Regulating SMC Growth." *Science Advances* 9, no. 35: eadh8939. https://doi.org/10.1126/sciadv.adh8939.

McMillin, M. A., G. A. Frampton, A. P. Seiwell, N. S. Patel, A. N. Jacobs, and S. DeMorrow. 2015. "TGFβ1 Exacerbates Blood–brain Barrier Permeability in a Mouse Model of Hepatic Encephalopathy via Upregulation of MMP9 and Downregulation of Claudin-5." *Laboratory Investigation* 95, no. 8: 903–913. https://doi.org/10.1038/labinvest.2015.70.

Moriwaki, K., C. Park, K. Koyama, S. Balaji, et al. 2022. "The Scaffold-Dependent Function of RIPK1 in Dendritic Cells Promotes Injury-Induced Colitis." *Mucosal Immunology* 15, no. 1: 84–95. https://doi.org/10.1038/s41385-021-00446-y.

Oerlemans, M. I. F. J., J. Liu, F. Arslan, et al. 2012. "Inhibition of RIP1-Dependent Necrosis Prevents Adverse Cardiac Remodeling After Myocardial Ischemia–Reperfusion In Vivo." *Basic Research in Cardiology* 107, no. 4: 270. https://doi.org/10.1007/s00395-012-0270-8.

Ofengeim, D., and J. Yuan. 2013. "Regulation of RIP1 Kinase Signalling at the Crossroads of Inflammation and Cell Death." *Nature Reviews Molecular Cell Biology* 14, no. 11: 727–736. https://doi.org/10.1038/nrm3683.

Orozco, S., N. Yatim, M. R. Werner, H. Tran, et al. 2014. "RIPK1 Both Positively and Negatively Regulates RIPK3 Oligomerization and Necroptosis." *Cell Death & Differentiation* 21, no. 10: 1511–1521. https://doi.org/10.1038/cdd.2014.76.

Pasparakis, M., and P. Vandenabeele. 2015. "Necroptosis and Its Role in Inflammation." *Nature* 517, no. 7534: 311–320. https://doi.org/10.1038/nature14191.

Prieto-Vila, M., Y. Yoshioka, N. Kuriyama, et al. 2024. "Adult Cardiomyocytes-Derived EVs for the Treatment of Cardiac Fibrosis." *Journal of Extracellular Vesicles* 13, no. 7: e12461. https://doi.org/10.1002/jev2.12461.

Reventun, P., M. Alique, I. Cuadrado, et al. 2017. "iNOS-Derived Nitric Oxide Induces Integrin-Linked Kinase Endocytic Lysosome-Mediated Degradation in the Vascular Endothelium." *Arteriosclerosis, Thrombosis, and Vascular Biology* 37, no. 7: 1272–1281. https://doi.org/10.1161/ATVBAHA.117.309560.

Reventun, P., S. Sánchez-Esteban, A. Cook-Calvete, M. Delgado-Marín, et al. 2023. "Endothelial ILK Induces Cardioprotection by Preventing Coronary Microvascular Dysfunction and Endothelial-to-Mesenchymal Transition." *Basic Research in Cardiology* 118, no. 1: 28. https://doi.org/10.1007/s00395-023-00997-0.

Riebeling, T., K. Jamal, R. Wilson, B. Kolbrink, et al. 2021. "Primidone Blocks RIPK1-driven Cell Death and Inflammation." *Cell Death & Differentiation* 28, no. 5: 1610–1626. https://doi.org/10.1038/s41418-020-00690-y.

Sánchez-Esteban, S., M. Castro-Pinto, A. Cook-Calvete, P. Reventún, et al. 2022. "Integrin-Linked Kinase Expression in Human Valve Endothelial Cells Plays a Protective Role in Calcific Aortic Valve Disease." *Antioxidants* 11, no. 9: 1736. https://doi.org/10.3390/antiox11091736.

Shlomovitz, I., Z. Erlich, G. Arad, L. Edry-Botzer, et al. 2021. "Proteomic Analysis of Necroptotic Extracellular Vesicles." *Cell Death & Disease* 12, no. 11: 1059. https://doi.org/10.1038/s41419-021-04317-z.

Suades, R., M. F. Greco, P. Prieto, et al. 2024. "CD66b$^+$ /CD68$^+$ Circulating Extracellular Vesicles, Lactate Dehydrogenase and Neutrophil-to-Lymphocyte Ratio Can Differentiate Coronavirus Disease 2019 Severity During and After Infection." *Journal of Extracellular Vesicles* 13, no. 7: e12456. https://doi.org/10.1002/jev2.12456.

Sun, W., H. Lu, L. Ma, C. Ding, H. Wang, and Y. Chu. 2024. "Deubiquitinase USP5 Regulates RIPK1 Driven Pyroptosis in Response to Myocardial Ischemic Reperfusion Injury." *Cell Communication and Signaling* 22, no. 1: 466. https://doi.org/10.1186/s12964-024-01853-x.

Taqueti, V. R., and M. F. Di Carli. 2018. "Coronary Microvascular Disease Pathogenic Mechanisms and Therapeutic Options." *Journal of the American College of Cardiology* 72, no. 21: 2625–2641. https://doi.org/10.1016/j.jacc.2018.09.042.

Tauro, B. J., D. W. Greening, R. A. Mathias, S. Mathivanan, H. Ji, and R. J. Simpson. 2013. "Two Distinct Populations of Exosomes Are Released from LIM1863 Colon Carcinoma Cell-derived Organoids." *Molecular & Cellular Proteomics* 12, no. 3: 587–598. https://doi.org/10.1074/mcp.M112.021303.

Tuttolomondo, A., M. Daidone, and A. Pinto. 2020. "Endothelial Dysfunction and Inflammation in Ischemic Stroke Pathogenesis." *Current Pharmaceutical Design* 26, no. 34: 4209–4219. https://doi.org/10.2174/1381612826666200417154126.

Wang, Q., T. Zhou, Z. Liu, J. Ren, et al. 2017. "Inhibition of Receptor-Interacting Protein Kinase 1 with Necrostatin–1s Ameliorates Disease Progression in Elastase-induced Mouse Abdominal Aortic Aneurysm Model." *Scientific Reports* 7, no. 1: 42159. https://doi.org/10.1038/srep42159.

Wehrens, X. 2000. "Mouse Electrocardiography an Interval of Thirty Years." *Cardiovascular Research* 45, no. 1: 231–237. https://doi.org/10.1016/S0008-6363(99)00335-1.

Welsh, J. A., D. C. I. Goberdhan, L. O'Driscoll, E. I. Buzas, et al. 2024. "Minimal Information for Studies of Extracellular Vesicles (MISEV2023): From Basic to Advanced Approaches." *Journal of Extracellular Vesicles* 13, no. 2: e12404. https://doi.org/10.1002/jev2.12404.

Welsh, J. A., E. Van Der Pol, G. J. A. Arkesteijn, M. Bremer, et al. 2020. "MIFlowCyt-EV: A Framework for Standardized Reporting of Extracellular Vesicle Flow Cytometry Experiments." *Journal of Extracellular Vesicles* 9, no. 1: 1713526. https://doi.org/10.1080/20013078.2020.1713526.

White, D. E., P. Coutu, Y. F. Shi, J. C. Tardif, et al. 2006. "Targeted Ablation of ILK from the Murine Heart Results in Dilated Cardiomyopathy and Spontaneous Heart Failure." *Genes & Development* 20, no. 17: 2355–2360. https://doi.org/10.1101/gad.1458906.

20013078, 2026, 6, Downloaded from https://isevjournals.onlinelibrary.wiley.com/doi/10.1002/jev2.70335 by Spanish Cochrane National Provision (Ministerio de Sanidad), Wiley Online Library on [31/07/2026]. See the Terms and Conditions (https://onlinelibrary.wiley.com/terms-and-conditions) on Wiley Online Library for rules of use; OA articles are governed by the applicable Creative Commons License

Williams, C., R. Pazos, F. Royo, E. González, et al. 2019. "Assessing the Role of Surface Glycans of Extracellular Vesicles on Cellular Uptake." *Scientific Reports* 9, no. 1: 11920. https://doi.org/10.1038/s41598-019-48499-1.

Wolf, M., R. W. Poupardin, P. Ebner-Peking, A. C. Andrade, et al. 2022. "A Functional Corona Around Extracellular Vesicles Enhances Angiogenesis, Skin Regeneration and Immunomodulation." *Journal of Extracellular Vesicles* 11, no. 4: e12207. https://doi.org/10.1002/jev2.12207.

Xu, S., I. Ilyas, P. J. Little, H. Li, et al. 2021. "Endothelial Dysfunction in Atherosclerotic Cardiovascular Diseases and Beyond: From Mechanism to Pharmacotherapies." *Pharmacological Reviews* 73, no. 3: 924–967. https://doi.org/10.1124/pharmrev.120.000096.

Yao, H., C. Huang, J. Zou, W. Liang, et al. 2024. "Extracellular Vesicle-Packaged lncRNA From Cancer-Associated Fibroblasts Promotes Immune Evasion by Downregulating HLA-A in Pancreatic Cancer." *Journal of Extracellular Vesicles* 13, no. 7: e12484. https://doi.org/10.1002/jev2.12484.

Yoshida, Y., and H. Nishi. 2022. "The Role of the Complement System in Kidney Glomerular Capillary Thrombosis." *Frontiers in Immunology* 13: 981375. https://doi.org/10.3389/fimmu.2022.981375.

Zhang, F., and F. Guo. 2018. "Effect of Transplantation of Cardiac Stem Cells Overexpressing Integrin-linked Kinase on Cardiac Function of Rats with Acute Myocardial Infarction." *Experimental and Therapeutic Medicine* 16, no. 5: 746–750. https://doi.org/10.3892/etm.2018.6198.

Zhang, X., J. Yang, S. Ma, X. Gao, et al. 2024. "Functional Diversity of Apoptotic Vesicle Subpopulations from Bone Marrow Mesenchymal Stem Cells in Tissue Regeneration." *Journal of Extracellular Vesicles* 13, no. 4: e12434. https://doi.org/10.1002/jev2.12434.

Zhang, Y., J. J. Li, R. Xu, X. P. Wang, et al. 2023. "Nogo-B Mediates Endothelial Oxidative Stress and Inflammation to Promote Coronary Atherosclerosis in Pressure-overloaded Mouse Hearts." *Redox Biology* 68: 102944. https://doi.org/10.1016/j.redox.2023.102944.

Zhu, C., L. Pan, F. Zhou, R. Mao, et al. 2024. "Urocortin2 attenuates Diabetic Coronary Microvascular Dysfunction by Regulating Macrophage Extracellular Vesicles." *Biochemical Pharmacology* 219: 115976. https://doi.org/10.1016/j.bcp.2023.115976.⟨/bib.

Supporting Information

Additional supporting information can be found online in the Supporting Information section.

Supporting information: jev270335-supp-0001-SuppMat.pdf **Supporting information**: jev270335-supp-0002-TablesS1-S3.docx

20013078, 2026, 6, Downloaded from https://isevjournals.onlinelibrary.wiley.com/doi/10.1002/jev2.70335 by Spanish Cochrane National Provision (Ministerio de Sanidad), Wiley Online Library on [31/07/2026]. See the Terms and Conditions (https://onlinelibrary.wiley.com/terms-and-conditions) on Wiley Online Library for rules of use; OA articles are governed by the applicable Creative Commons License